

The Broad-band X-ray Spectrum of IC 4329A from a Joint *NuSTAR*/*Suzaku* Observation

L. W. Brenneman¹, G. Madejski², F. Fuerst³, G. Matt⁴, M. Elvis¹, F. A. Harrison³,
D. R. Ballantyne⁵, S. E. Boggs⁶, F. E. Christensen⁷, W. W. Craig^{7,8}, A. C. Fabian⁹,
B. W. Grefenstette³, C. J. Hailey¹⁰, K. K. Madsen³, A. Marinucci⁴, E. Rivers³, D. Stern¹¹,
D. J. Walton³, W. W. Zhang¹²

ABSTRACT

We have obtained a deep, simultaneous observation of the bright, nearby Seyfert galaxy IC 4329A with *Suzaku* and *NuSTAR*. Through a detailed spectral analysis, we are able to robustly separate the continuum, absorption and distant reflection components in the spectrum. The absorbing column is found to be modest ($\sim 6 \times 10^{21} \text{ cm}^{-2}$), and does not introduce any significant curvature in the Fe K band. We are able to place a strong constraint on the presence of a broadened Fe K α line ($E_{\text{rest}} = 6.46_{-0.07}^{+0.08} \text{ keV}$ with $\sigma = 0.33_{-0.07}^{+0.08} \text{ keV}$ and $EW = 34_{-7}^{+8} \text{ eV}$), though we

¹Harvard-Smithsonian CfA, 60 Garden St. MS-67, Cambridge, MA 02138, USA

²Kavli Institute for Particle Astrophysics and Cosmology, SLAC National Accelerator Laboratory, Menlo Park, CA 94025, USA

³Cahill Center for Astronomy and Astrophysics, California Institute of Technology, Pasadena, CA 91125, USA

⁴Dipartimento di Matematica e Fisica, Università Roma Tre, via della Vasca Navale 84, I-00146 Roma, Italy

⁵Center for Relativistic Astrophysics, School of Physics, Georgia Institute of Technology, Atlanta, GA 30332, USA

⁶Space Science Laboratory, University of California, Berkeley, California 94720, USA

⁷DTU SpaceNational Space Institute, Technical University of Denmark, Elektrovej 327, 2800 Lyngby, Denmark

⁸Lawrence Livermore National Laboratory, Livermore, California 94550, USA

⁹Institute of Astronomy, Madingley Road, Cambridge CB3 0HA, UK

¹⁰Columbia Astrophysics Laboratory, Columbia University, New York, New York 10027, USA

¹¹Jet Propulsion Laboratory, California Institute of Technology, Pasadena, CA 91109, USA

¹²NASA Goddard Space Flight Center, Greenbelt, Maryland 20771, USA

are not able to constrain any of the parameters of a relativistic reflection model. These results highlight the range in broad Fe K line strengths observed in nearby, bright AGN (roughly an order of magnitude), and imply a corresponding range in the physical properties of the inner accretion disk in these sources. We have also updated our previously reported measurement of the high-energy cutoff of the hard X-ray emission using both observatories rather than just *NuSTAR* alone: $E_{\text{cut}} = 186 \pm 14 \text{ keV}$. This high-energy cutoff acts as a proxy for the temperature of the coronal electron plasma, enabling us to further separate this parameter from the plasma’s optical depth and to update our results for these parameters as well. We derive $kT = 50_{-3}^{+6} \text{ keV}$ with $\tau = 2.34_{-0.11}^{+0.16}$ using a spherical geometry, $kT = 61 \pm 1 \text{ keV}$ with $\tau = 0.68 \pm 0.02$ for a slab geometry, with both having an equivalent goodness-of-fit.

1. Introduction

X-ray observations of active galactic nuclei (AGN) elucidate many physical processes that drive the production of high-energy photons close to a supermassive black hole (SMBH). In addition to probing the properties of the corona in radio-quiet AGN, X-ray data can constrain the nature of the inner accretion flow by measuring the morphology of the Fe K α line. This emission line, with a rest energy of 6.4 keV for neutral iron, arises via fluorescence from the accretion disk, which is illuminated by the Compton-scattered continuum X-rays. Given the relatively high cosmic abundance of iron and its high fluorescent yield, coupled with the lack of other lines expected in that part of the spectrum, it is a reasonably “clean” probe of the kinematics of the accreting material.

Narrow (usually unresolved by CCD detectors, i.e., $v/c \lesssim 0.005$) Fe K α lines have been observed in the vast majority of Seyfert galaxies (Yaqoob & Padmanabhan 2004). In addition to their small width, the lack of variability implies that they originate from the illumination by the primary X-ray source of reprocessing material relatively far from the black hole, likely in the outer disk or torus of Seyfert unification schemes (Antonucci 1993; Urry & Padovani 1995). Indeed, this emission region has been spatially resolved in the Seyfert 2 AGN NGC 4945 (Marinucci et al. 2012), and it lies at a distance from the nucleus of 30 – 50 pc ($\sim 10^8 - 10^9 r_g$ for the $10^6 M_\odot$ black hole at its core, where $r_g \equiv GM/c^2$). The near ubiquity of these features suggests that this distant material is present in almost all Seyfert AGN. In some Seyfert galaxies the Fe K line appears to be broadened (to $v/c \gtrsim 0.1$), most likely by relativistic effects; e.g., MCG–6–30–15, first observed by Tanaka et al. (1995), and recently also confirmed in NGC 1365 (Risaliti et al. 2013). These sources are two of

the best examples of AGN displaying a prominent red wing indicative of fluorescing material close to the innermost stable circular orbit (ISCO) in the accretion disk.

A broad Fe $K\alpha$ line originating from material extending to the ISCO allows us to determine whether the black hole is rotating, and if so, to determine its spin and possibly direction as well (for recent reviews, see, e.g., Reynolds 2013 and Brenneman 2013). However, such broad, relativistic emission lines are not observed in all Seyferts observed with high signal-to-noise (S/N) (Nandra et al. 2007; de La Calle Pérez et al. 2010; Brenneman et al. 2012), possibly indicating the absence of relatively cold, Compton-thick gas close to the black hole (though the caveats to line detection detailed in Ballantyne 2010 should also be kept in mind).

Regardless of the mechanism by which they are determined, any inferences regarding the structure, location, and physical conditions of the accretion disk and the corona require a precise, high S/N measurement of the broad-band X-ray spectrum from ≤ 2 to ≥ 50 keV. This is necessary in order to disentangle various emission and absorption components contributing to the total observed X-ray emission, described above. A significant advance towards such measurements is provided by the deployment of the focusing hard X-ray telescopes onboard the *NuSTAR* observatory, the latest in the series of NASA’s Small Explorer satellites. This mission is sensitive in the bandpass of 3 – 79 keV with the updated calibration, and provides a hundredfold improvement of sensitivity in the hard X-ray band over previous instruments (Harrison et al. 2013). The use of *NuSTAR* in conjunction with X-ray telescopes that are more sensitive at softer energies (e.g., *XMM-Newton* and *Suzaku*) yields the highest S/N ever achieved across the $\sim 0.2 - 79$ keV bandpass.

Equally important in deriving the physical properties of the disk and corona is the selection of a representative, bright target. One good candidate is the southern Seyfert 1.2 galaxy IC 4329A ($z = 0.0161$, Willmer et al. 1991; $N_{\text{H}} [\text{gal}] = 4.61 \times 10^{20} \text{ cm}^{-2}$, Kalberla et al. 2005; $M_{\text{BH}} = 1.20 \times 10^8 M_{\odot}$, de La Calle Pérez et al. 2010), which in the hard X-ray/soft γ -ray band appears similar to an average radio-quiet Seyfert (e.g., Zdziarski et al. 1996). The host galaxy is an edge-on spiral in a pair with IC 4329, separated by ~ 3 arcmin. IC 4329A was one of the first AGN observed to have a Compton reflection component in addition to its strong Fe $K\alpha$ line (Piro, Yamauchi, & Matsuoka 1990). As with most other X-ray emitting Seyferts, it is variable, but the variability amplitude during a typical observation is modest: the root mean square fractional variability has been measured at $\leq 20\%$ in the 15 – 150 keV *RXTE* band (Markowitz 2009), and $(17 \pm 3)\%$ in the 14 – 195 keV band with *Swift*/BAT (Soldi et al. 2014). The average 2 – 10 keV flux historically ranges from $F_{2-10} \sim (0.1 - 1.8) \times 10^{-10} \text{ erg cm}^{-2} \text{ s}^{-1}$ (Beckmann et al. 2006; Verrecchia et al. 2007). IC 4329A has been the subject of many X-ray observations, beginning with the

analysis of its simultaneous *ROSAT* and *OSSE* spectrum (Zdziarski 1994; Madejski et al. 1995). In harder X-rays, the source has also been observed by *BeppoSAX* (Perola et al. 2002), *ASCA+RXTE* (Done, Madejski, & Życki 2000) and *INTEGRAL* (Molina et al. 2013), which have placed rough constraints on the high-energy cutoff of the power-law (a proxy for coronal temperature) at $E_{\text{cut}} \geq 180$ keV, $E_{\text{cut}} = 150 - 390$ keV and $E_{\text{cut}} = 60 - 300$ keV, respectively. Combining the non-simultaneous *INTEGRAL* and *XMM-Newton* data further constrained the cutoff energy to $E_{\text{cut}} = 130 - 203$ keV (Molina et al. 2009), while a combination of the *XMM* and *BeppoSAX* data yielded $E_{\text{cut}} = 150 - 390$ keV (Gondoin et al. 2001).

A detailed examination of the *ASCA* and simultaneous *RXTE* data revealed that the continuum is indeed described well by the model used to describe the *ROSAT+OSSE* data (either thermal or non-thermal Comptonization plus neutral, distant reflection), and that the Fe K α line is moderately broadened and can be described by a Gaussian with FWHM of $\sim 30,000$ km s $^{-1}$ (Done et al. 2000). This is consistent with the conclusions of Dadina (2007), who noted a moderately broad Fe K α line of similar width and equivalent widths up to $EW \sim 180$ eV in *BeppoSAX* data, paired with measured reflection fractions up to $R \sim 1.5$. Both the *ASCA* and *ROSAT* data, as well as the *XMM-Newton* observations (Steenbrugge et al. 2005), suggest that the soft X-ray spectrum is absorbed by a combination of neutral and partially ionized gas, with a total column of $\sim 3 \times 10^{21}$ cm $^{-2}$. This is comparable to the host galaxy’s ISM column density (Wilson & Penston 1979). After accounting for the reflection component, the source shows some modest spectral variability of the primary continuum, being softer at higher flux levels (Madejski, Done, & Życki 2001; Miyazawa, Haba, & Kunieda 2009; Markowitz 2009).

Here, we report on results from our simultaneous *Suzaku* and *NuSTAR* observation of IC 4329A. We discussed our measurements of the properties of the underlying continuum in Brenneman et al. (2014) (hereafter referred to as paper I), and in this work we update those values and focus on constraining the reprocessing components. In §2, we report on the *Suzaku* and *NuSTAR* observations, and in §3 we present a brief timing analysis of the data. Our spectral analysis follows in §4, with a discussion of the inferred accretion disk properties and their implications in §5.

2. Observations and Data Reduction

IC 4329A was observed quasi-continuously and contemporaneously by *Suzaku* and *NuSTAR* from August 12-16, 2012 in normal clocking mode. The observations had a roughly 50% efficiency due to Earth occultations. After eliminating Earth occultations, passages through the South Atlantic Anomaly (SAA) and other periods of high background, the

Suzaku observation totaled ~ 118 ks of on-source time from August 13-15, while the *NuSTAR* observation totaled ~ 160 ks of on-source time from August 12-16. Count rates, total counts and signal-to-noise (S/N) ratio for each instrument from the two observatories is listed in Table 1.

The *Suzaku*/XIS data were taken with the telescope at the XIS nominal aimpoint, and were reduced as per the ABC Guide¹, using the latest versions of the CALDB (October 2013) and HEASoft (v6.15) packages as of the time of this writing. After reprocessing the data from XIS 0, XIS 1 and XIS 3 (XIS 2 has been inoperable since November 2006) using the `aepipeline` script, source and background regions were extracted for each detector within XSELECT. Source regions were circular and 160 arcseconds in radius centered on the source, while background regions were extracted from as much of the surrounding region on the same chip as possible, avoiding the source region and the calibration sources in the detector corners. We then generated response matrices using the `xisresp` script at “medium” speed, after which we combined the data from the front-illuminated (FI) XIS 0 and XIS 3 detectors using the `addascaspec` script in order to maximize S/N. The XIS source and background spectra, as well as the responses, were then grouped to a minimum of 25 counts per channel in order to facilitate robust χ^2 fitting. For all of the spectral fitting presented later in §4, we evaluate the combined XIS-FI with the XIS 1 spectra between $0.7 - 1.5$ and $2.5 - 10$ keV. The $1.5 - 2.5$ keV range is ignored due to the presence of calibration features. We allow for a global flux cross-normalization error between the XIS-FI and XIS 1 spectra, fitting it as a free parameter. At 0.975 ± 0.005 , we find it slightly lower than the published value of the XIS 1 cross-normalization relative to the combined XIS-FI data (1.019 ± 0.010).²

The HXD/GSO detection of IC 4329A was marginal, but corresponds, very roughly, to $F_{50-150} \sim 10^{-10}$ erg cm $^{-2}$ s $^{-1}$ in the 50 – 150 keV band. With such a weak detection, we did not use the GSO data in our analysis.

Data from the HXD/PIN instrument were again reduced and reprocessed as per the *Suzaku* ABC Guide. For background subtraction, we used the “tuned” non X-ray background (NXB) event file for August 2012 from the *Suzaku* CALDB, along with the appropriate response file and flat field file for epoch 11 data. We modeled the cosmic X-ray background (CXB) contribution as per the ABC Guide, simulating its spectrum in XSPEC (Arnaud 1996). The simulated CXB spectrum (modeled as in Boldt 1987) contributed a count rate of $(14.7 \pm 0.1) \times 10^{-3}$ cts s $^{-1}$ to the total X-ray background from 16 – 60 keV, coupled with a source count rate of $(268 \pm 3) \times 10^{-3}$ cts s $^{-1}$ over this range. The NXB and CXB files

¹<http://heasarc.gsfc.nasa.gov/docs/suzaku/analysis/abc/>

²<http://heasarc.gsfc.nasa.gov/docs/suzaku/analysis/watchout.html>

were combined to form a single PIN background spectrum. Because the PIN data only contain 256 spectral channels (vs. the 4096 channels in the unbinned XIS data), rebinning to 25 counts per bin was not necessary in order to facilitate χ^2 fitting. Rather, we rebinned the PIN spectrum to have a S/N of 5 in each energy bin, which limited our energy range to 16 – 60 keV. We also added 3% systematic errors to the PIN data to account for the uncertainty in the non-X-ray background data supplied by the *Suzaku* calibration team. For most of the spectral fitting presented in this paper, we assume a PIN/XIS-FI cross-normalization factor of 1.164 ± 0.014 as per the *Suzaku* memo 2008-06³, though we allow the factor to vary around this value. The fitted value is 1.217 ± 0.024 .

The *NuSTAR* data were collected with the two focal plane module telescopes (FPMA and FPMB) centered roughly ~ 2 arcmin from the nucleus of IC 4329A. We reduced the data using the *NuSTAR* Data Analysis Software (NUSTARDAS) and calibration version 1.1.1⁴. We filtered the event files and applied the default depth correction using the `nupipeline` task. The source and background regions were circles of radius 75 arcsec, with the source region centered on IC 4329A and the background region taken from the corner of the same detector, as close as possible to the source without being contaminated by the PSF wings. Spectra and light curves were extracted and response files were generated using the `nuproducts` task. In order to minimize systematic effects, we have not combined responses or spectra from FPMA and FPMB; instead, we fit them simultaneously. We allow the cross-normalization factor between each module and the *Suzaku*/XIS-FI data to fit freely. The absolute cross-calibration factor is 1.092 ± 0.018 for FPMA and 1.166 ± 0.020 for FPMB. We obtain excellent agreement in the expected spectral shape below 10 keV, where there is good overlap between *Suzaku*/XIS and *NuSTAR*/FPMA and FPMB: when fit with a simple power-law model, the photon index for the *NuSTAR* detectors is $\Gamma = 1.687 \pm 0.002$, while that of *Suzaku*/XIS is $\Gamma = 1.690 \pm 0.003$.

For all the analysis presented here, we used XRONOS version 5.22 and XSPEC version 12.8.1, along with other FTOOLS packages within HEASoft 6.14. Uncertainties quoted within the text are at the 1σ level of confidence, unless otherwise specified, while those in tables are quoted at 90% confidence.

³<http://heasarc.gsfc.nasa.gov/docs/suzaku/analysis/watchout.html>

⁴<http://heasarc.gsfc.nasa.gov/docs/nustar/>

3. Timing Analysis

IC 4329A showed a modest, secular flux evolution during the joint *Suzaku*/*NuSTAR* observing campaign, roughly consistent with previous observations (Markowitz & Edelson 2004). In both datasets, the source flux increased by $\sim 12\%$ over the first 50 ks of the exposure, then plateaued at the maximum count rate for ~ 50 ks before decreasing by $\sim 34\%$ over the remainder of the observation (clock time is used to measure these intervals). No significant flux variability was seen on short timescales in any of the instruments. Background levels were approximately constant, except for a factor ~ 3 flare in *Suzaku*/XIS 1 seen in the last time bin (see Fig. 1). On average, the $2 - 10$ keV flux during our observations was comfortably within the historical range⁵: $1.02 \times 10^{-10} \text{ erg cm}^{-2} \text{ s}^{-1}$ vs. $(0.1 - 1.8) \times 10^{-10} \text{ erg cm}^{-2} \text{ s}^{-1}$.

The hardness ratio in the XIS was nearly constant over the observation (Fig. 2), taken between the $2 - 5$ keV and $5 - 10$ keV bands. During the final ~ 50 ks the hardness did increase by $\sim 13\%$ as the source continued to decrease in flux by $\sim 19\%$ over the same time interval. The *NuSTAR* data show a similar overall trend, visually, but the total amount of flux variability is significantly lower at these higher energies ($10 - 30$ keV vs. $30 - 79$ keV) as compared with the *Suzaku*/XIS data. The hardness ratio taken from the *NuSTAR* data is consistent with a constant value (Fig. 2).

To assess the amount of variability in our observations in a model-independent way, we also calculated the root mean square fractional variability vs. energy of the combined *Suzaku*/XIS data as well as the *NuSTAR*/FPMA and FPMB data. This fractional variability spectrum, or $\text{RMS } F_{\text{var}}$, is derived using the methods described in Edelson et al. (2002) and Vaughan et al. (2003), and the results are plotted in Fig. 3. The source shows the expected decrease in overall fractional source variability with energy due to a combination of the increasing relative importance of reflection from distant matter (Niedźwiecki & Miyakawa 2010) as well as the decreasing importance of the power-law component. We also note that both the *Suzaku* and *NuSTAR* data display a prominent dip between $6 - 7$ keV, roughly coincident with the Fe $K\alpha$ line thought to arise from the fluorescence of distant material due to irradiation by the primary X-ray source. If this emitting gas is located at many thousands of gravitational radii from the corona, as described in AGN unification schemes, it would not vary on the timescales of our observing campaign, meaning that we should expect to see such a dip in the $\text{RMS } F_{\text{var}}$ spectrum.

Given the lack of short timescale variability in our observations of IC 4329A, along with

⁵<http://ned.ipac.caltech.edu/>

its overall modest flux and hardness ratio changes, we use the time-averaged spectrum in all of the broad band spectral fitting (§4.1-4.2). A discussion of the modest spectral variability is deferred to §4.3.

4. Spectral Analysis

We begin our analysis of the time-averaged spectrum of IC 4329A with an examination of the *Suzaku*/XIS spectrum from 0.7 – 10.0 keV (ignoring the energy range from 1.5 – 2.5 keV due to calibration uncertainties around the Si edge). We constrain the properties of the continuum and get a preliminary assessment of the contributions of complex absorption intrinsic to the AGN, distant reflection from the outer disk and/or torus, and relativistic inner disk reflection. We then add in the *Suzaku*/PIN data from 16 – 60 keV to aid in constraining the slope of the power-law continuum and the fractional contribution of reflection.

We continue our analysis by including the *NuSTAR*/FPMA and FPMB data, which have significantly better signal-to-noise and reduced systematic error than the PIN above 10 keV, and to access energies out to 79 keV that are unreachable by the *Suzaku*/PIN instrument. The use of simultaneous *Suzaku* and *NuSTAR* data allows us to better constrain the parameters of the continuum and reflection, and to constrain the cutoff energy of the power-law component. The importance of having broadband, high S/N X-ray spectra from both observatories lies in our enhanced ability to break modeling degeneracies, and to therefore constrain the physical parameters of three main spectral components with enough accuracy and precision to yield the best estimates of the temperature and optical depth of the coronal plasma taken to date.

We also consider the spectral variability of the source, examining the high-flux vs. low-flux spectra in order to understand the physical processes driving the flux evolution in IC 4329A.

4.1. A First Look at the *Suzaku* Spectra

The *Suzaku*/XIS-FI and XIS 1 data between 2.5 – 5 keV and 7.5 – 10 keV are well fit by a power-law of slope $\Gamma = 1.66 \pm 0.01$ modified by a Galactic column of $N_{\text{H}} = 4.61 \times 10^{20} \text{ cm}^{-2}$ (Kalberla et al. 2005). Here we use the **TBabs** model of Wilms, Allen, & McCray (2000), along with abundances set to **wilm** (Wilms et al. 2000) and cross-section table set to **vern** (Verner et al. 1996). Strong residuals remain when the entire bandpass is considered, however (the XIS 1 data are ignored above 7 keV due to a rapid loss in detector sensitivity above this energy). Below 2 keV, these residuals take the form of a pronounced dip below the

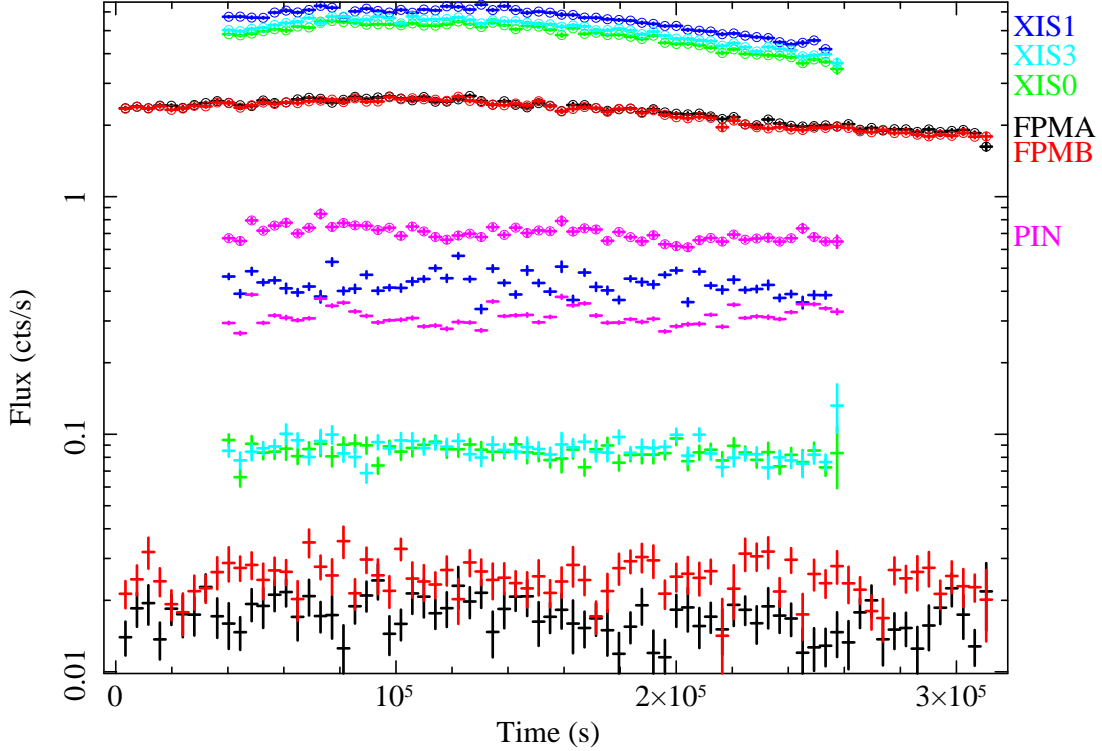


Fig. 1.— Simultaneous source and background light curves from the six instruments on *Suzaku* and *NuSTAR* that observed IC 4329A simultaneously in 2012, integrated over all energies for each detector. Source counts are shown with crosses in circles, background counts with plain crosses. Black data points show the *NuSTAR*/FPMA data, red show the FPMB data, green show the *Suzaku*/XIS 0 data, dark blue show the XIS 1 data, light blue show the XIS 3 data, and magenta show the HXD/PIN data. Background colors match the source colors and the vertical order of appearance is the same as for the source data points, except for the PIN background, which is second from the top of the background data points.

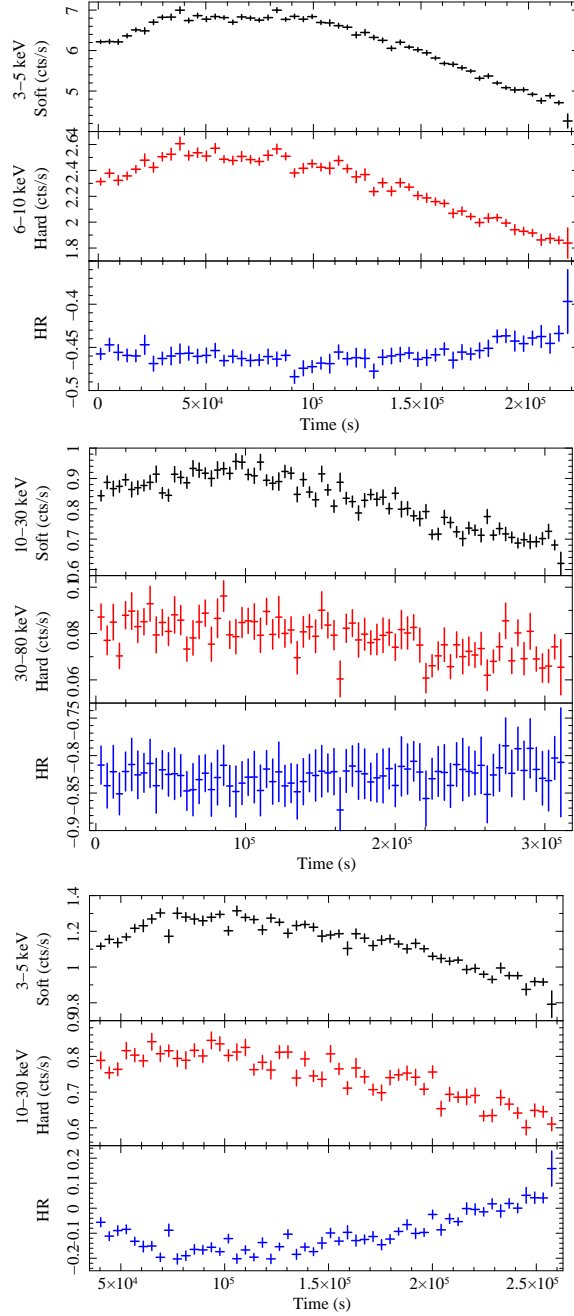


Fig. 2.— *Top:* Simultaneous light curves and hardness ratio for the combined *Suzaku*/XIS data at a resolution of 4096 sec/bin. The top panel shows the 3 – 5 keV data, middle shows the 6 – 10 keV data and bottom shows the hardness ratio between them, computed as $(H-S)/(H+S)$, where H and S denote the hard and soft count rates, respectively. *Middle:* The same plot, this time for the *NuSTAR*/FPMA data using 10 – 30 keV for the soft data and 30 – 79 keV for the hard data. The FPMB light curves and hardness ratio are virtually identical to those from FPMA, so are not shown here. *Bottom:* The same plot, this time comparing the 10 – 30 keV *NuSTAR*/FPMA light curve to the 3 – 5 keV light curve taken from *Suzaku*/XIS 3. The light curves are required to be strictly simultaneous and are normalized by their effective areas in the given energy ranges in order to account for the differences between instruments.

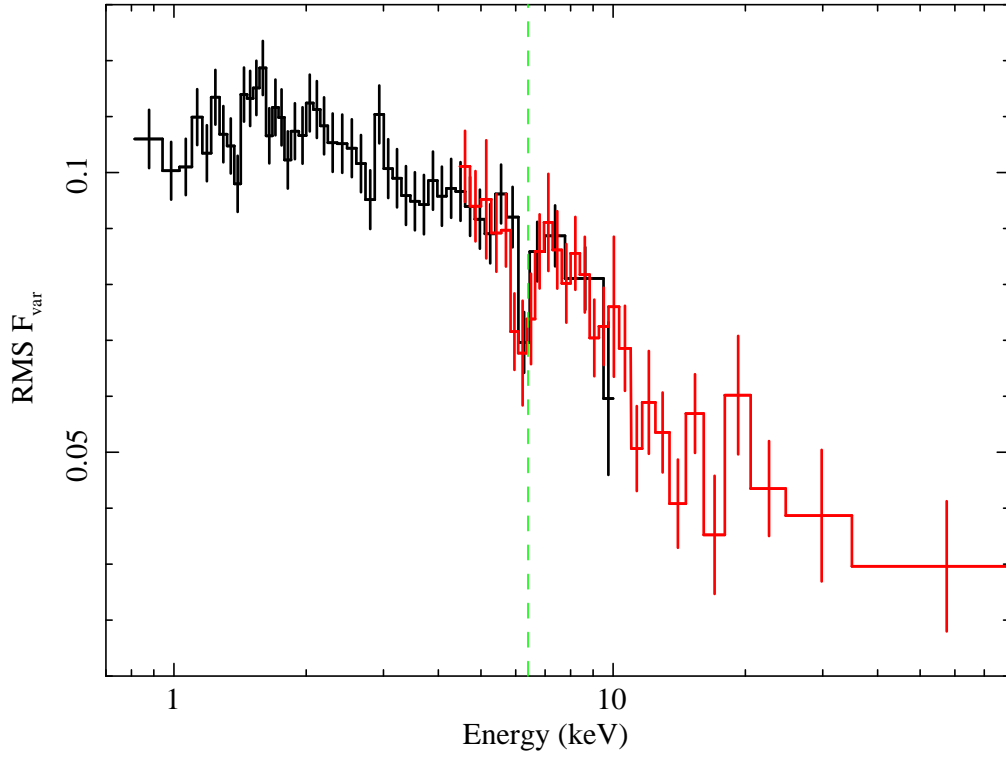


Fig. 3.— Root mean square fractional variability vs. energy for the *Suzaku*/XIS-FI (black) and *NuSTAR*/FPMA (red) data (FPMB is omitted for clarity, but overlaps with FPMA). Note the prominent, sharp dip in $\text{RMS } F_{\text{var}}$ at ~ 6.4 keV, the rest-frame energy of the Fe $K\alpha$ line (this energy is marked with the dashed green line). This dip indicates that the narrow Fe $K\alpha$ line is less variable than the surrounding continuum, as one would expect if it originates from gas that is distant from the source of the hard X-rays.

ideal data/model ratio of unity, indicating the presence of a significant column of absorbing gas along the line of sight to the AGN. The initial power-law model has a global goodness-of-fit of $\chi^2/\nu = 444071/2147$ (207). The spectral fit improves dramatically with the addition of an XSTAR (Kallman & Bautista 2001) warm absorber table in which the absorbing gas has a column density of $N_{\text{H}} = (5.9 \pm 0.1) \times 10^{21} \text{ cm}^{-2}$ and an ionization parameter of $\log \xi = 0.80 \pm 0.01 \text{ erg cm s}^{-1}$: this results in $\chi^2/\nu = 3558/2145$ (1.66).

An emission line-like feature remains in the residuals at $0.78 \pm 0.01 \text{ keV}$. This feature can be modeled with a Gaussian that likely represents a blend of the resonance, intercombination and forbidden O VII emission lines. The spectral resolution of the *Suzaku*/XIS instrument is insufficient to separate these three putative lines, however, so it is not possible to derive a density or temperature for the emitting gas via line ratios. This residual feature also does not appear to be a simple consequence of using only one layer of intervening gas to describe the intrinsic absorption of the source, since adding in a second absorber does not improve the fit, nor does it mitigate this feature. If modeled with a Gaussian, the line has a width of $\sigma = 0.02 \pm 0.01 \text{ keV}$ ($\text{FWHM} \sim 18,000 \pm 9000 \text{ km s}^{-1}$; well within the Broad Emission Line Region, though if this is a line blend any velocity inferred from its width would be erroneous) and a strength relative to the continuum of $EW = 39 \pm 6 \text{ eV}$. Adding in this feature further improves the fit to $\chi^2/\nu = 3151/2142$ (1.47). The succession of data-to-model ratios from the simple power-law and absorbed power-law models is shown in Fig. 4, which also highlights the putative O VII line and the residuals in the Fe K band.

Above 5 keV, the Fe K emission complex is clearly present, with a prominent, narrow Fe K α line at $6.41 \pm 0.04 \text{ keV}$ and perhaps a blend of Fe K β and Fe XXVI at $6.99 \pm 0.03 \text{ keV}$ (Fig. 4). Though there is a visual suggestion of an Fe XXV emission line at $\sim 6.7 \text{ keV}$, including a Gaussian at this energy does not improve the fit. The iron edge is also clearly seen at $7.25 \pm 0.07 \text{ keV}$, perhaps indicating a slightly ionized disk, consistent with the possible presence of an ionized iron line at $\sim 7 \text{ keV}$. No strong, broadened emission in the Fe K band is immediately apparent to the eye, though there are indications of a possible Compton shoulder or iron line red wing at $6.2 \pm 0.04 \text{ keV}$. If we use Gaussian emission lines and an absorption edge to parametrize these features and require that all the Fe K emission features have the same width as the narrow Fe K α line, we obtain a width of $\sigma = 0.05 \pm 0.01 \text{ keV}$, $EW_{\text{K}\alpha} = 64 \pm 6 \text{ eV}$, $EW_{\text{FeXXVI/K}\beta} = 12 \pm 3 \text{ keV}$, and $EW_{\text{CS}} = 13 \pm 4 \text{ eV}$. The goodness-of-fit for the 0.7 – 10 keV XIS spectra including these components is $\chi^2/\nu = 2162/2133$ (1.01).

Substituting a broad Gaussian emission line at 6.4 keV in place of the Compton shoulder results in the same overall goodness-of-fit, with the width of the broad line at $\sigma = 0.33 \pm 0.09 \text{ keV}$. This corresponds to $\text{FWHM} \sim 36,000 \pm 9800 \text{ km s}^{-1}$, placing the origin of the line at $r \sim 70 \pm 19 r_{\text{g}}$, if the width of the line corresponds to a Keplerian velocity in the

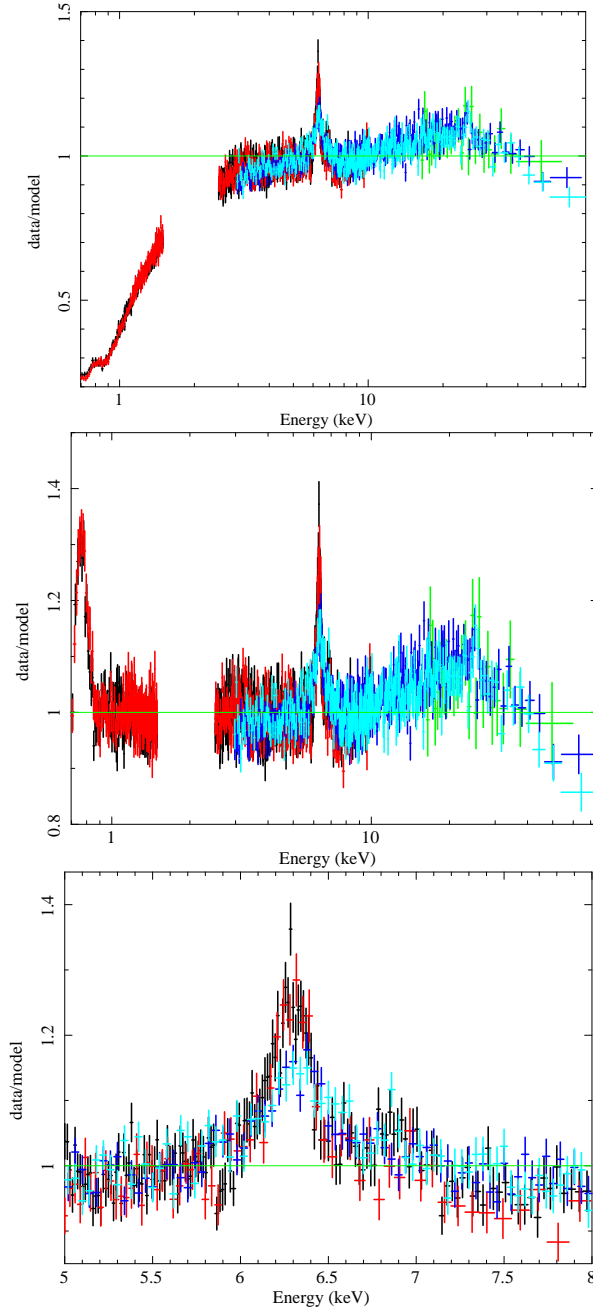


Fig. 4.— *Top:* The ratio of the spectrum of IC 4329A to a power-law modified by Galactic photoabsorption. Co-added *Suzaku*/XIS-FI data are in black, XIS 1 data are in red, HXD/PIN data are in green, *NuSTAR*/FPMA data are in dark blue, and FPMB data are in light blue. The horizontal green line represents a perfect fit, or a data-to-model ratio of unity. *Middle:* Same plot as above, but absorption intrinsic to the AGN is now included in the model, eliminating the curvature below 2 keV. *Bottom:* A zoomed-in version of the middle plot, focused on the Fe K region.

disk. This velocity is consistent with that found by Shu, Yaqoob, & Wang (2010) using *Chandra*/HETG data, and is ~ 5 times greater than that of the $H\beta$ line in IC 4329A ($FWHM = 5620 \pm 200 \text{ km s}^{-1}$; Shu et al. 2010 and references therein). This implies that the X-ray broad line emission region (BELR) is ~ 5 times closer to the black hole than the optical BELR. The inclusion of a relativistic line via the **relline** model (Dauser et al. 2010) does not improve the fit, however, and the **relline** parameters are unconstrained except for the normalization. We note that the joint *ASCA* and *RXTE* analysis of IC 4329A by Done et al. (2000) included a similar broadening of the Fe $K\alpha$ line, but likewise could not definitively conclude an inner disk origin for this feature. We proceed under the assumption that the excess emission redward of 6.4 keV is either a Compton shoulder or a modest contribution from inner disk reflection. Its equivalent width is $EW = 36 \pm 8 \text{ eV}$ in the case of a broad Gaussian at $6.38 \pm 0.02 \text{ keV}$.

Adding in the HXD/PIN data from 16 – 60 keV, we notice convex curvature that peaks around $\sim 25 \text{ keV}$ and tails off at higher energies, suggesting the presence of the Compton reflection continuum and a high-energy cutoff to the power-law component, as found in paper I. The addition of the unmodeled PIN data results in a predictable worsening of the goodness-of-fit to $\chi^2/\nu = 2267/2201$ (1.03) before refitting, and $\chi^2/\nu = 2248/2201$ (1.02) after refitting. Including a **pexrav** component (Magdziarz & Zdziarski 1995) with $R = 0.19 \pm 0.05$ recovered the $\leq 10 \text{ keV}$ fit of $\chi^2/\nu = 2230/2203$ (1.01). We note that this reflection includes both a contribution from the neutral outer disk or torus, as well as the inner disk (if present). The inclination angle was unconstrained in the fit, so we fixed it to $i = 60^\circ$; this is the typical value assumed for the average over a distribution of disks at random angles. We elected to keep the cutoff energy of the illuminating power-law fixed at 300 keV, since the limited energy range and high background of the PIN data render them of limited use in probing this parameter.

For a more self-consistent approach, we then replaced the Gaussians-plus-**pexrav** model with a **pexmon** component (Nandra et al. 2007), which calculates the expected Fe K emission signatures (Fe $K\alpha$, $K\beta$ and the Compton shoulder, as well as Ni $K\alpha$ and $K\beta$) and the corresponding Compton hump together. We fixed the cutoff energy of the power-law for the **pexmon** model at 300 keV. Allowing the iron abundance to fit freely, we obtained $R = 0.21 \pm 0.04$ and $\text{Fe/solar} = 1.56 \pm 0.64$, for a goodness-of-fit of $\chi^2/\nu = 2229/2203$ (1.01). The inclination angle was fixed to $i = 60^\circ$ as in the **pexrav** fit. Including Gaussian emission lines for Fe xxv and xxvi did not statistically improve the fit, though they did lessen the residuals in these regions to the eye. A visual inspection of the residuals also indicated that the region from 6.0 – 6.4 keV was underfitted by the model. Given that **pexmon** includes a Compton shoulder already, we infer that this excess emission likely corresponds to a modest broad Fe K line. Parametrizing this component with a Gaussian emission line at $6.36 \pm 0.03 \text{ keV}$ yields

an equivalent width of $EW = 34 \pm 7$ eV, consistent with its value above, and also shows a similar line width.

Replacing the **pexmon** component with the more physically realistic XSTAR-generated **xillver** model of García et al. (2014) yields a similar goodness-of-fit, with $\chi^2/\nu = 2227/2200$ (1.01) for $\text{Fe}/\text{solar} = 1.3 \pm 0.5$ and $K_{\text{refl}} = (4.50 \pm 1.38) \times 10^{-5} \text{ ph cm}^{-2} \text{ s}^{-1}$ (roughly equivalent to $R = 0.20$ in **pexmon**). The ionization we find is low but unconstrained, so we elected to fix it at the neutral value. The inclination angle of the reprocessor to the line of sight was similarly unconstrained, so we fixed it to $i = 60^\circ$. As with the **pexmon** model, **xillver** underestimated the amount of emission between 6.0–6.4 keV in spite of having the Compton shoulder included in the model; including an additional Gaussian component at $E = 6.43 \pm 0.04$ keV (rest frame) with $EW = 41 \pm 6$ eV corrected this issue.

4.2. Joint Analysis of the *Suzaku* and *NuSTAR* Spectra

Including the *NuSTAR* data with our *Suzaku* data, along with their appropriate cross-normalization factors, yields the highest S/N ever achieved across the 0.7 – 79 keV energy range. This enables us to probe the change in shape of the continuum at high energies, as well as the contribution from reflection above 10 keV and in the Fe K band simultaneously.

We plot the ratio of the *Suzaku*/XIS-FI, XIS-BI and HXD/PIN spectra, along with the *NuSTAR*/FPMA and FPMB spectra to a power-law continuum modified by Galactic photoabsorption in Fig. 4. The same residuals detailed in §4.1 are seen, but the curvature above 10 keV is now well-defined as a result of the higher S/N *NuSTAR* data.

A rollover at high energies is visually evident even from the *Suzaku*/PIN data, and becomes clearly evident when the FPMA and FPMB spectra are added to the already-modeled *Suzaku* data, even though reflection is already included in the model (see Fig. 5). The presence of this feature contributes to a global fit of $\chi^2/\nu = 4793/4341$ (1.10). We now allow the high-energy cutoff to the power-law and **xillver** reflection components to vary freely in order to assess the robustness of such a feature over and above the distant reflection, and, if present, to constrain its cutoff energy. This approach improves the fit to $\chi^2/\nu = 4557/4340$ (1.05) and greatly improves the data-to-model ratio at high energies as well, visually. The cutoff energy of the power-law is constrained to $E_{\text{cut}} = 186 \pm 14$ keV. In comparison, paper I yielded $E_{\text{cut}} = 178_{-40}^{+74}$ keV with *NuSTAR* alone. The residuals around the narrow Fe K α line necessitate the addition of a broader Gaussian component, as described in §4.1. The best-fitting rest-frame energy of this line is $E = 6.46 \pm 0.08$ keV, with equivalent width $EW = 34 \pm 7$ eV. We will refer to this model as Model 1 throughout the rest of the

paper.

Given the high S/N out to 79 keV achievable with *NuSTAR*, we can consider more physically motivated models to describe the continuum emission than the more phenomenological cutoff power-law. To this end, in paper I we employed the `compTT` model of Titarchuk (1994), parametrizing the continuum as being produced by inverse Compton scattering of thermal disk photons off of relativistic electrons situated above the disk in either a slab or spherical geometry.

We adopt a similar approach in modeling the combined dataset here, applying a `compTT` model component to the combined *Suzaku*+*NuSTAR* spectra, rather than a phenomenological power-law continuum. The rest of the model components remained the same: the `xillver` component used for the reflected emission had its incident power-law spectral index frozen to the best-fit value obtained in Model 1, much like the approach taken using the `compTT` model in paper I. The spherical corona geometry is hereafter referred to as Model 2, while the slab geometry is Model 3. Plots of the contributions of individual model components to the overall fit are shown in Fig. 6.

Model 2 yields a goodness-of-fit of $\chi^2/\nu = 4550/4344 (1.05)$, while Model 3 produces $\chi^2/\nu = 4555/4344 (1.05)$; in comparison Model 1 comes to $\chi^2/\nu = 4558/4344 (1.05)$. None of the common parameter values change significantly between models. The power-law of Model 1 finds its best fit with $\Gamma = 1.73 \pm 0.01$ and $E_{\text{cut}} = 186 \pm 14$ keV, while the Comptonization components of Models 2-3 return coronal temperatures and optical depths of $kT = 50^{+6}_{-3}$ keV and 61 ± 1 keV and $\tau = 2.34^{+0.16}_{-0.21}$ and 0.68 ± 0.02 , respectively. In comparison, in paper I the *NuSTAR* data alone returned $kT = 33 \pm 6$ keV and 37^{+3}_{-6} keV and $\tau = 3.41^{+0.58}_{-0.38}$ and $1.25^{+0.20}_{-0.10}$ for each model. We will discuss these differences further in §5

The Markov Chain Monte Carlo (MCMC) analysis used to measure the formal distribution of each parameter across its available parameter space for each model was performed using the Metropolis-Hastings algorithm (e.g., Kashyap & Drake 1998 and references therein) with four chains of 55,000 elements, in which the first 5000 elements from each were discarded as part of the “burn-in” period. Each chain was started at a random seed in the global parameter space using a diagonal covariance matrix with Gaussian errors derived from the squares of the 1σ errors from the model fitting in XSPEC. The rescaling factor of the covariance matrix was derived using trial and error based on an initial estimate of $1/N^2$, where N is the number of free parameters in the fit. The appropriate rescaling factor was determined by ensuring that the fraction of repeated values in a given chain was approximately 75%. The Gelman–Rubin convergence criterion of ~ 1 was achieved for each chain.⁶

⁶As outlined in the XSPEC manual: <http://heasarc.gsfc.nasa.gov/docs/xanadu/xspec/manual/XSchain.html>

Instrument	Exposure (ks)	Count Rate (cts/s)	Total Counts	S/N
<i>Suzaku</i> /XIS 0	118	3.792 ± 0.006	448,350	629
<i>Suzaku</i> /XIS 1	118	3.732 ± 0.006	442,833	652
<i>Suzaku</i> /XIS 3	118	3.980 ± 0.006	470,300	644
<i>Suzaku</i> /PIN	106	0.268 ± 0.003	53,426	5
<i>NuSTAR</i> /FPMA	162	2.608 ± 0.004	426,274	653
<i>NuSTAR</i> /FPMB	159	2.513 ± 0.004	403,588	645

Table 1: Observation details for the *Suzaku* and *NuSTAR* campaign on IC 4329A. Exposure times, count rates, total counts and S/N are taken from the background-subtracted data. Energy ranges for the XIS detectors are 0.7 – 1.5 and 2.5 – 10 keV, 16 – 60 keV for the PIN, and 3 – 79 keV for the FPMA and FPMB data. Signal-to-noise was calculated for the unbinned spectra over the given energy bands using the source-dominated case described in Longair (2011) for the XIS, FPMA and FPMB. The PIN data were background-dominated and thus rebinned to $S/N = 5$.

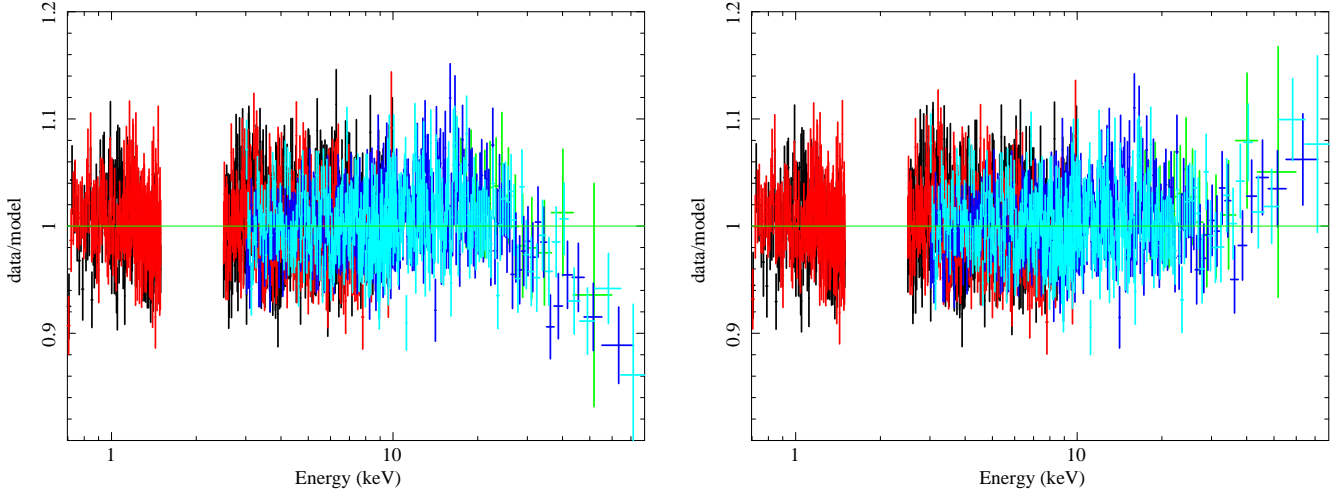


Fig. 5.— *Left*: Data-to-model ratio for the best-fitting `xillver`+power-law model applied to the *Suzaku* data, now with data from *NuSTAR*/FPMA and FPMB added in and refitting performed. Note the rollover of the spectra above 25 keV. *Right*: The data-to-model ratio for Model 1, incorporating distant reflection through `xillver`, a power-law continuum, and a high-energy cutoff.

Once each chain run was completed, the four chains were loaded back into XSPEC to create a composite 200,000-element chain used to extract 90% confidence errors (shown in Table 2) and to examine the distribution of each individual parameter in the fit. We then generated probability density contours for the most interesting pairs of parameters for each model, which are shown in Figs. 7, 8 and 9.

The best-fit parameters and their MCMC-derived 90% confidence errors from all three models are shown in Table 2. The total absorbed 2–10 keV flux and luminosity of the model are $F_{2-10} = 1.04 \times 10^{-10} \text{ erg cm}^{-2} \text{ s}^{-1}$ and $L_{2-10} = 6.03 \times 10^{43} \text{ erg s}^{-1}$, respectively, while their unabsorbed values are $F_{2-10} = 1.08 \times 10^{-10} \text{ erg cm}^{-2} \text{ s}^{-1}$ and $L_{2-10} = 6.26 \times 10^{43} \text{ erg s}^{-1}$.

4.3. Spectral Variability

Our simultaneous *Suzaku* and *NuSTAR* observations of IC 4329A do not show marked variability on short timescales, as exhibited by many other AGN (e.g., NGC 1365, Risaliti et al. 2013). Nonetheless, it is useful to examine time-sliced spectra from the highest and lowest flux states of the source during our campaign. This exercise yields insight into the changes in certain spectral components driving the change in flux, i.e., to what degree these flux changes are caused by variations in the continuum, absorption or reflection components.

We extracted simultaneous high- and low-flux spectra from the time intervals in each observation (*Suzaku*/XIS-FI and *NuSTAR*/FPMA; FPMB are not shown for clarity, but are virtually identical to FPMA). These spectra are shown in Fig. 10. The high-flux state spectra totaled 46 ks of exposure time and represent the highest source flux with simultaneous data from the two telescopes. The low-flux state totaled 63 ks of exposure time, and represents the lowest source flux with simultaneous data from both telescopes. Difference spectra were created by subtracting the low-flux spectra from the high-flux spectra in both *Suzaku*/XIS-FI and *NuSTAR*/FPMA. We show all six spectra plotted against the best-fit power-law modified by Galactic photoabsorption in Fig. 11. Note that the difference spectra show no change from the high- and low-state spectra below $\sim 2 \text{ keV}$, indicating the constancy of the warm absorber during our observations. Close inspection of Fig. 11 also reveals that the reflection features (Fe K band and Compton hump above 10 keV) are slightly more prominent during the low-flux state when the power-law emission is minimized. The difference spectra show no residual reflection features, implying that these are constant in flux over the course of the observation. We can therefore infer that changes in only the power-law flux drive the slight spectral evolution that takes place as IC 4329A transitions from a higher-flux state to a lower-flux state during our campaign.

Component	Parameter (units)	Model 1	Model 2	Model 3
TBabs	N_{H} (cm $^{-2}$)	$4.61 \times 10^{20}(f)$	$4.61 \times 10^{20}(f)$	$4.61 \times 10^{20}(f)$
XSTAR grid	N_{H} (cm $^{-2}$)	$6.03 \pm 0.13 \times 10^{21}$	$6.02 \pm 0.13 \times 10^{21}$	$6.00^{+0.12}_{-0.13} \times 10^{21}$
	$\log \xi$ (erg cm s $^{-1}$)	0.73 ± 0.02	0.73 ± 0.02	0.73 ± 0.02
zpo	Γ	1.73 ± 0.01	$1.73(f)$	$1.73(f)$
	E_{cut} (keV)	186^{+14}_{-14}	— — —	— — —
	K_{po} (ph cm $^{-2}$ s $^{-1}$)	$2.82 \pm 0.03 \times 10^{-2}$	— — —	— — —
compTT	kT_e (keV)	— — —	50^{+6}_{-3}	61 ± 1
	τ	— — —	$2.34^{+0.16}_{-0.21}$	0.68 ± 0.02
	K_{comptt} (ph cm $^{-2}$ s $^{-1}$)	— — —	$5.46^{+0.38}_{-0.54} \times 10^{-3}$	$4.46 \pm 0.11 \times 10^{-3}$
xillver	Fe/solar	$1.51^{+0.29}_{-0.28}$	$1.51^{+0.28}_{-0.27}$	$1.50^{+0.28}_{-0.27}$
	Γ	$1.73*$	$1.73(f)$	$1.73(f)$
	K_{refl} (ph cm $^{-2}$ s $^{-1}$)	$2.79 \pm 0.20 \times 10^{-4}$	$2.74 \pm 0.18 \times 10^{-4}$	$2.89 \pm 0.18 \times 10^{-4}$
zgauss	E_1 (keV)	0.78 ± 0.01	0.78 ± 0.01	0.78 ± 0.01
	σ_1 (keV)	$2.04^{+0.50}_{-0.67} \times 10^{-2}$	$1.97^{+0.49}_{-0.57} \times 10^{-2}$	$2.17^{+0.43}_{-0.70} \times 10^{-2}$
	K_1 (ph cm $^{-2}$ s $^{-1}$)	$1.52^{+0.19}_{-0.25} \times 10^{-3}$	$1.48^{+0.23}_{-0.22} \times 10^{-3}$	$1.57^{+0.21}_{-0.25} \times 10^{-3}$
	EW_1 (eV)	36^{+5}_{-6}	37 ± 6	37^{+5}_{-6}
zgauss	E_2 (keV)	$6.46^{+0.08}_{-0.07}$	$6.46^{+0.09}_{-0.07}$	$6.46^{+0.08}_{-0.07}$
	σ_2 (keV)	$0.33^{+0.08}_{-0.07}$	$0.33^{+0.09}_{-0.07}$	$0.33^{+0.09}_{-0.07}$
	K_2 (ph cm $^{-2}$ s $^{-1}$)	$3.95^{+1.05}_{-1.08} \times 10^{-5}$	$3.84^{+1.05}_{-1.03} \times 10^{-5}$	$3.91 \pm 1.04 \times 10^{-5}$
	EW_2 (eV)	34^{+8}_{-7}	27^{+7}_{-6}	26 ± 7
Final fit		4558/4344 (1.05)	4550/4344 (1.05)	4555/4344 (1.05)

Table 2: Best-fit parameters, their values and uncertainties (to 90% confidence) for Models 1-3 fit to the *Suzaku*+*NuSTAR* data (see text for model details). Parameters marked with an (f) are held fixed in the fit, while those marked with an (*) are tied to another parameter (see text). Redshifts are fixed at the cosmological value for IC 4329A ($z = 0.0161$) unless otherwise specified. The warm absorber is assumed to totally cover the source and to have solar abundances. The **xillver** model for distant reflection has a photon index tied to that of the primary continuum and an ionization fixed to its lowest possible value ($\log \xi = 0$). Its inclination angle to the line of sight is fixed to 60° .

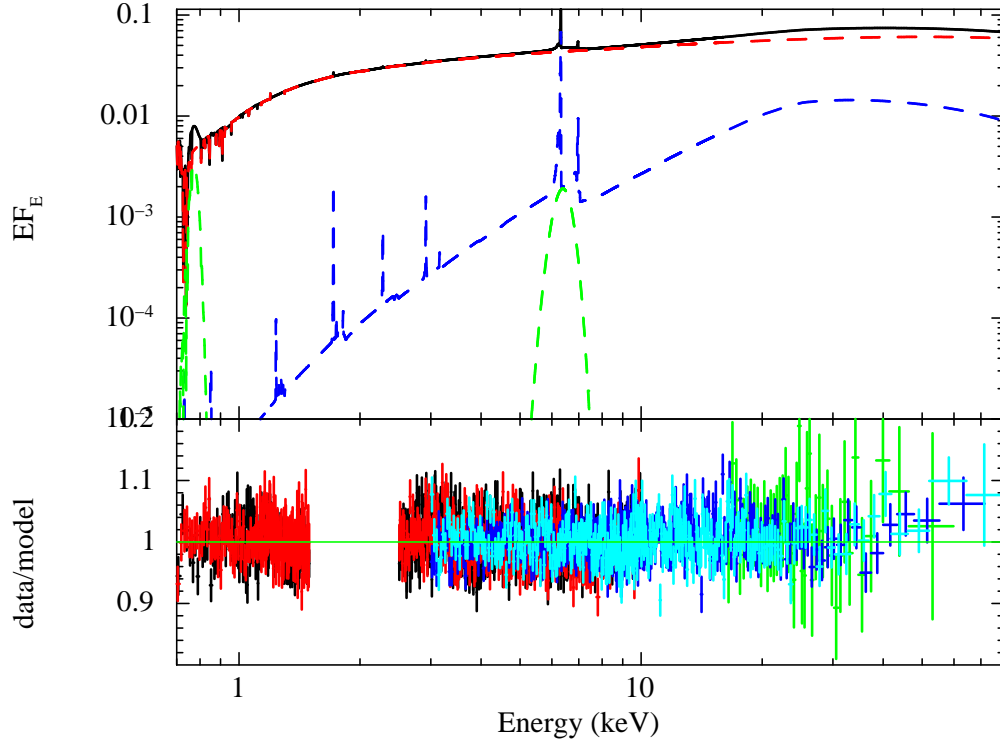


Fig. 6.— Best-fit components for Model 1. The cutoff power-law continuum (modified by the warm absorber below ~ 2 keV) is shown in red, the distant reflection (also modified by the absorber) in dark blue, and the Gaussian lines of O VII and Fe K are shown in green. The summed model is in black. Models 2-3 are virtually identical to Model 1 — replacing the power-law with the `compTT` Comptonization component — and so are not included here.

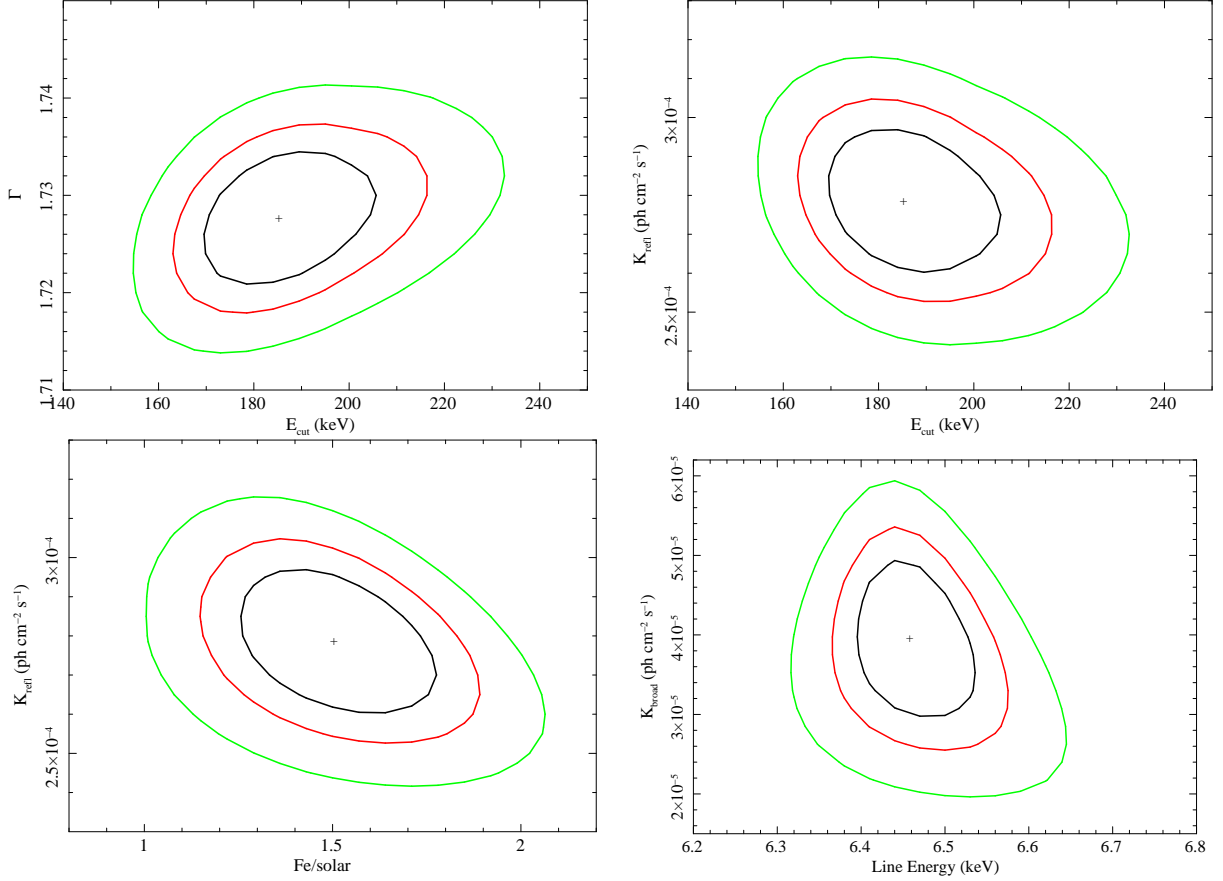


Fig. 7.— Contour plots from the MCMC analysis of Model 1, which show that, in each plot, the parameters are independently constrained and non-degenerate. *Top left:* 67%, 90% and 99% confidence contours showing the constraints on the photon index vs. cutoff energy of the power-law component. *Top right:* The normalization of the distant reflector (a proxy for reflection fraction) vs. the cutoff energy of the power-law component. Normalization is in units of ph cm $^{-2}$ s $^{-1}$. *Bottom left:* The iron abundance vs. normalization of the distant reflector. *Bottom right:* The rest-frame line centroid energy vs. normalization for the broad Fe K α line component, also in ph cm $^{-2}$ s $^{-1}$.

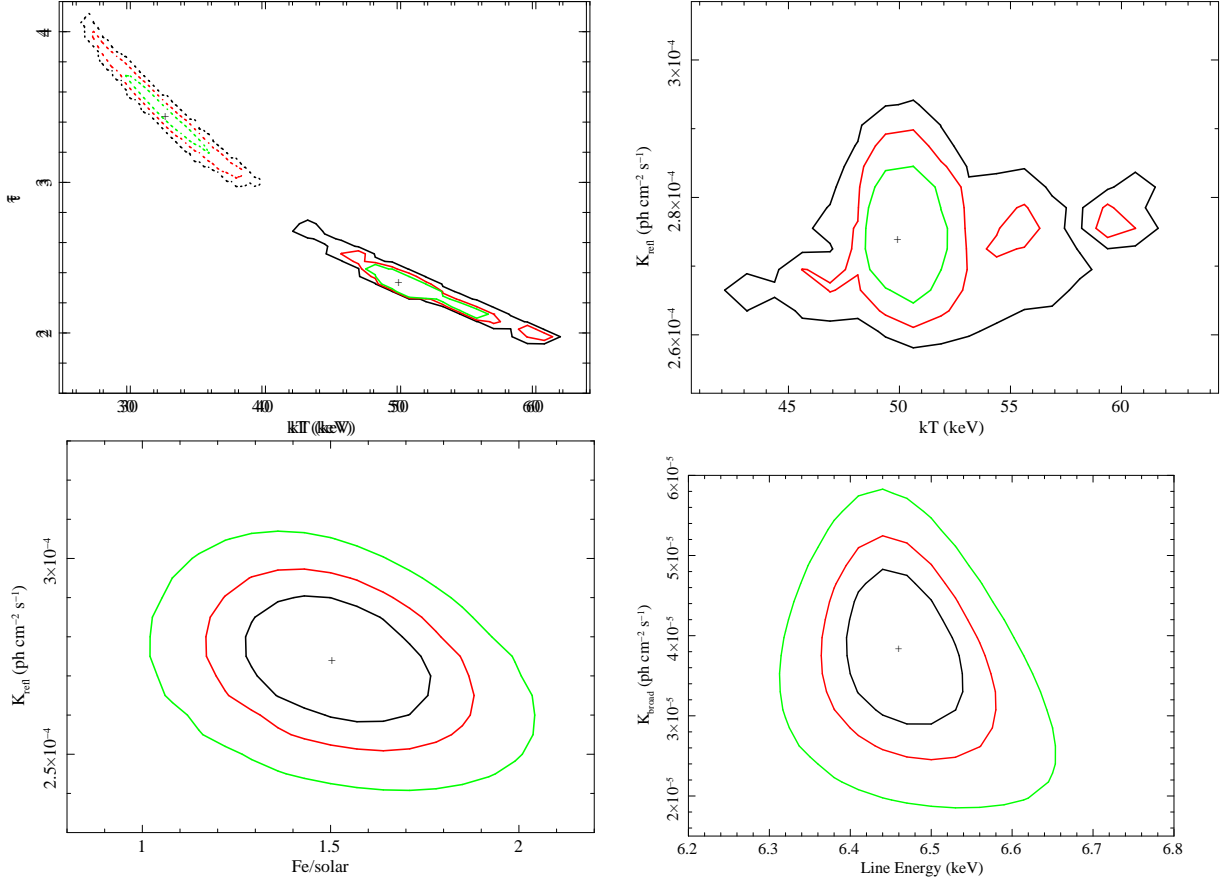


Fig. 8.— Contour plots from the MCMC analysis of Model 2. *Top left*: 67%, 90% and 99% confidence contours showing the constraints on the coronal plasma temperature and optical depth for the spherical geometry for the *NuSTAR*-only (dotted) and *NuSTAR*+*Suzaku* (solid) data. Though both parameters are constrained, there is still a clear degeneracy between the two. *Top right*: Normalization of the distant reflector vs. plasma temperature, with normalization in units of $\text{ph cm}^{-2} \text{s}^{-1}$. In this case the parameters are independently constrained and non-degenerate. *Bottom left*: The iron abundance vs. normalization of the distant reflector. *Bottom right*: The rest-frame line centroid energy vs. normalization for the broad Fe $K\alpha$ line component.

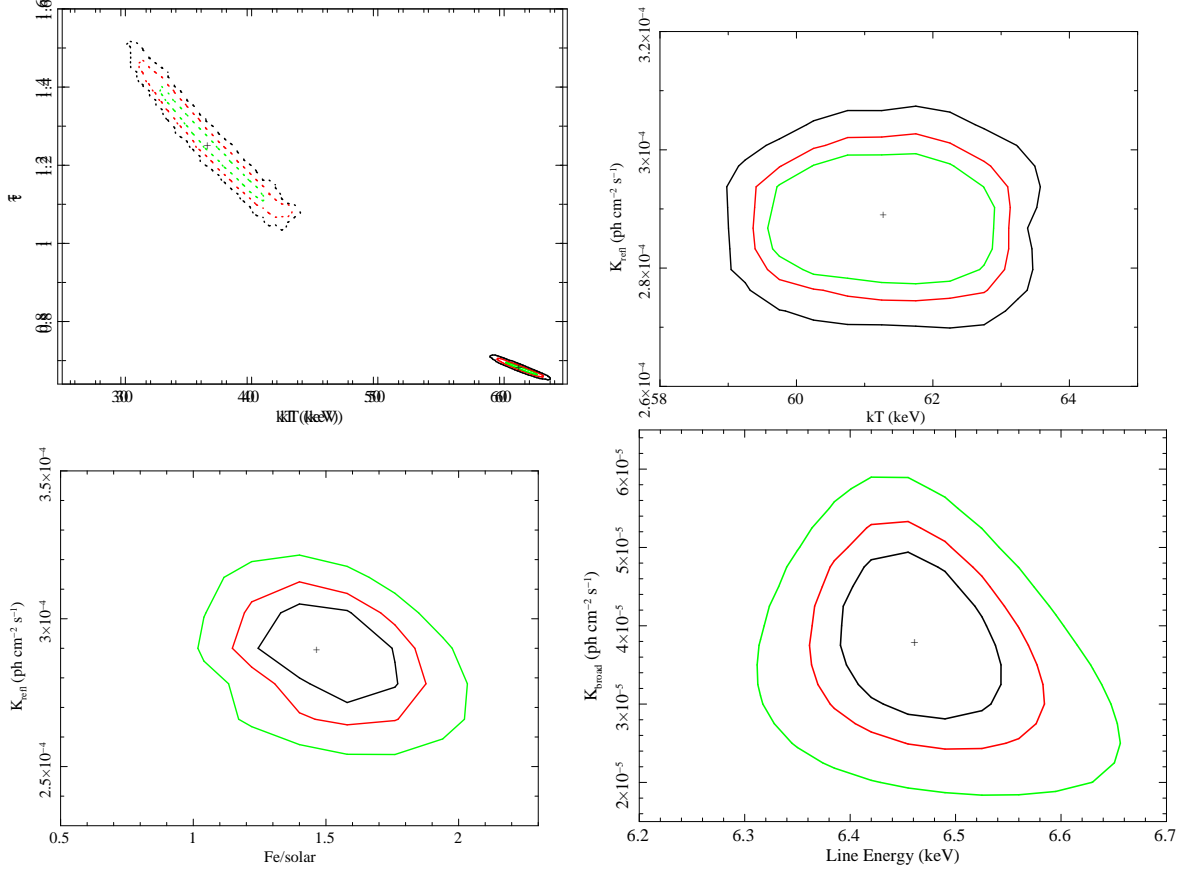


Fig. 9.— Contour plots from the MCMC analysis of Model 3. *Top left*: 67%, 90% and 99% confidence contours showing the constraints on the coronal plasma temperature and optical depth for the spherical geometry for the *NuSTAR*-only (dotted) and *NuSTAR*+*Suzaku* (solid) data. Though both parameters are constrained, there is still a clear degeneracy between the two. *Top right*: Normalization of the distant reflector vs. plasma temperature, with normalization in units of ph cm⁻² s⁻¹. In this case the parameters are independently constrained and non-degenerate. *Bottom left*: The iron abundance vs. normalization of the distant reflector. *Bottom right*: The rest-frame line centroid energy vs. normalization for the broad Fe K α line component.

The source is softer when brighter, as is typical in many actively accreting AGN: $\Gamma = 1.73 \pm 0.01$ in the high-flux state ($K_{\text{po}} = 3.01 \times 10^{-2} \text{ ph cm}^{-2} \text{ s}^{-1}$) vs. $\Gamma = 1.68 \pm 0.01$ in the low-flux state ($K_{\text{po}} = 2.23 \times 10^{-2} \text{ ph cm}^{-2} \text{ s}^{-1}$). This observed relation is thought to arise due to a correlation between the mass accretion rate and power-law slope, wherein higher accretion rates result in steeper spectra. This result can be explained if the Compton amplification factor decreases proportionally with the accretion rate in AGN (e.g., Sobolewska & Papadakis 2009 and references therein), though note all AGN display this behavior (e.g., NGC 4151; Lubiński et al. 2010).

The cutoff energy of the power-law in our data does not vary significantly from its best-fit value between the high- and low-flux spectra, and cannot be constrained in the difference spectrum. The difference spectrum is well fit by a power-law modified by both Galactic and intrinsic absorption, much like that described in the Model 1. This power-law has a slope of $\Gamma = 1.79 \pm 0.02$ and a normalization of $K_{\text{po}} = 7.84 \times 10^{-3} \text{ ph cm}^{-2} \text{ s}^{-1}$.

5. Discussion

5.1. Summary

In our deep observation of IC 4329A, performed simultaneously with *Suzaku* and *NuSTAR*, we are able to robustly separate the continuum, absorption and distant reflection components in the spectrum using the broad energy range of our observations. The results of our analysis can be summarized as follows:

- IC 4329A was viewed in a flux state near its historical average, and displayed little variability on short timescales and $\sim 30\%$ variability over the course of the campaign, **as has been found in previous X-ray observations.**
- While we were able to place a strong constraint on the presence of a broadened Fe $K\alpha$ line in the data ($EW = 34_{-9}^{+6} \text{ eV}$ in Model 1, the highest equivalent width seen in our modeling), we were not able to constrain any of the parameters when a relativistic line model was applied to the data. As such, it is not possible to derive any constraints on the spin of the black hole in IC 4329A using these observations.
- We have made the most accurate, precise measurement of the high-energy cutoff of the X-ray emission to date: $E_{\text{cut}} = 186 \pm 14 \text{ keV}$. This measurement improves on that made with *NuSTAR* alone in paper I ($E_{\text{cut}} = 178_{-40}^{+74} \text{ keV}$), demonstrating the necessity of obtaining high-S/N, broadband X-ray data in order to determine the properties of the corona.

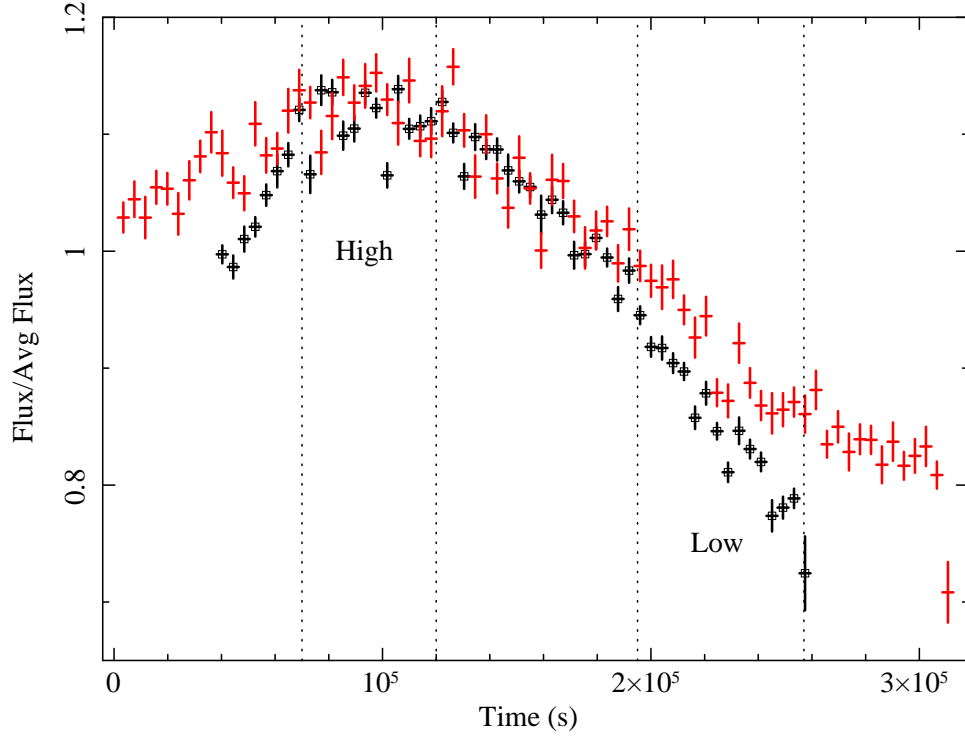


Fig. 10.— High- and low-flux time intervals common to the *Suzaku* and *NuSTAR* observations. *Suzaku*/XIS 3 data (0.7 – 10 keV) are shown in black (with square markers), *NuSTAR*/FPMA data (3 – 79 keV) in red (crosses), each normalized by their mean count rate to show the similarity in shape between the light curves.

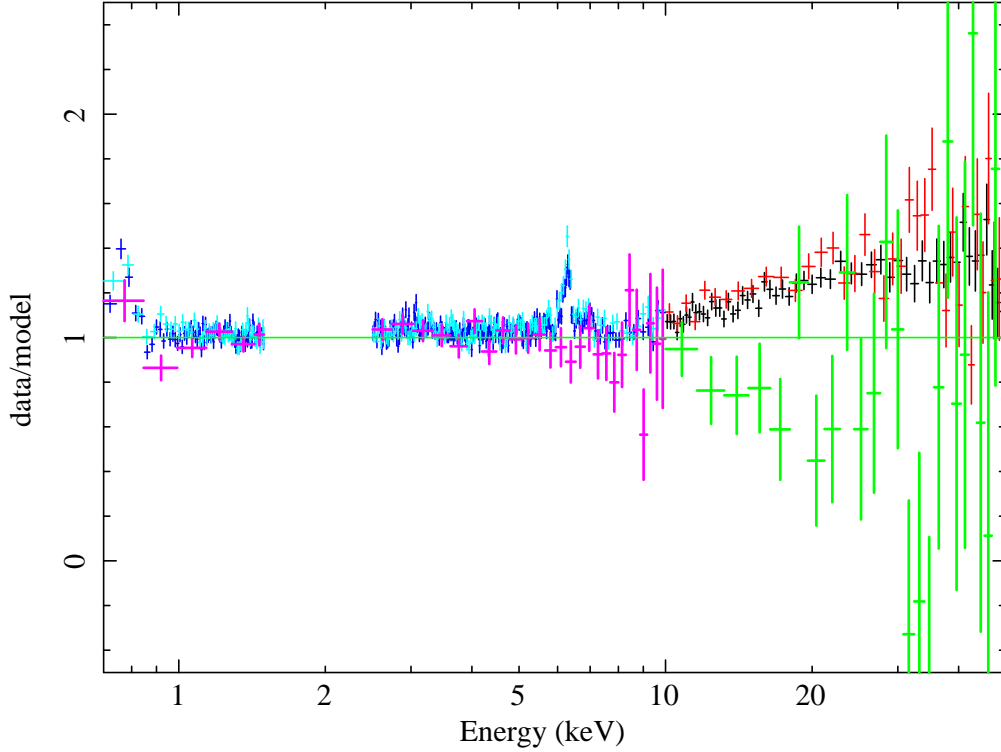


Fig. 11.— High-flux, low-flux and difference spectra from *Suzaku*/XIS-FI and *NuSTAR*/FPMA ratioed against a photoabsorbed power-law. Note the lack of reflection features evident in the residuals for the difference spectra. This is a strong indication that the power-law is driving the spectral changes over the course of the observation. The *Suzaku* high-flux spectrum is in dark blue, the low-flux spectrum is in light blue and the difference spectrum is in magenta. The *NuSTAR* high-flux spectrum is in black, the low-flux spectrum is in red and the difference spectrum is in green. The difference spectra are more coarsely binned for visualization purposes, and have larger uncertainties indicative of the marginal differences between the high and low flux states of IC 4329A, especially above 10 keV.

- Using data from both *Suzaku* and *NuSTAR*, we derive $kT = 50_{-3}^{+6}$ keV and $\tau = 2.34_{-0.21}^{+0.16}$ for the spherical geometry, with $kT = 61 \pm 1$ keV and $\tau = 0.68 \pm 0.02$ for the slab geometry.

5.2. Understanding the Corona

It is important to establish the continuum level in AGN in order to determine their overall energy budget, and the high-S/N, broadband X-ray spectra we have obtained using *Suzaku* and *NuSTAR* simultaneously enable us to disentangle the continuum, absorption and reflection signatures more accurately than we are able to with either observatory alone.

Our spectral and timing analyses of the simultaneous *Suzaku* and *NuSTAR* observations of IC 4329A demonstrate that changes in the continuum flux are responsible for the modest, secular changes in the overall source flux that we detect. The high-S/N, broadband spectra enable us to determine that neither the absorption nor reflection components show any significant variability over the course of our observing campaign. Though this result was hinted at in paper I, the addition of the *Suzaku* data to the analysis confirms the lack of absorption variability, in particular. Referencing Model 1, we note that the power-law normalization decreases by $\sim 30\%$ between the high- and low-flux states during our observations (§4.3); similarly, the overall source flux decreases by approximately the same amount (§3). The variation is more pronounced at energies below ~ 10 keV (Fig. 11), in keeping with our examination of the RMS variability spectrum (Fig. 3).

We note that the spectrum is rather hard: the cutoff power-law fit in Model 1 returns a photon index of $\Gamma = 1.73 \pm 0.01$, also confirming the results from paper I. This is consistent with several recent measurements taken with *Chandra* and *XMM* (average $\Gamma = 1.73$; McKernan & Yaqoob 2004; Steenbrugge et al. 2005; Markowitz, Reeves, & Braitto 2006), but inconsistent with the joint *XMM+INTEGRAL* spectral fitting performed by Molina et al. (2009) ($\Gamma = 1.81 \pm 0.03$). We note, however, that the data reported by Molina et al. were not obtained simultaneously. Spectral fitting returned a significantly softer index in previous epochs as well; between 1995 and 2001, the average reported spectral slope was $\Gamma = 1.91$ with a range between $\Gamma = 1.83 - 2.0$ (Madejski et al. 1995; Cappi et al. 1996; Perola et al. 1999; Done et al. 2000; Gondoin et al. 2001). Caution should be used when measuring the power-law slope using only data ≤ 10 keV, as the true slope of the continuum is best assessed over a much broader energy band extending out to higher energies where the continuum is more dominant. We also note that the quality of our data at high energies with *NuSTAR* now far surpasses that of the spectra obtained with *RXTE*, *BeppoSAX*, *CGRO* or *INTEGRAL*. Even so, these differences in measured power-law slope may indicate that IC 4329A

undergoes significant coronal variability on \leq years-long timescales.

It would be interesting to investigate whether the cutoff energy of the power-law shows similar variations to the spectral index, but unfortunately the constraints placed on this parameter historically are too loose to enable this test. In all of the observations prior to 2009, either the cutoff energy was fixed to the $E_{\text{cut}} = 270^{+167}_{-80}$ keV result obtained by Perola et al. (1999), or did not improve on this result (e.g., $E_{\text{cut}} \geq 100$ keV, Madejski et al. 1995; $E_{\text{cut}} = 270 \pm 120$ keV, Gondoin et al. 2001). Our result ($E_{\text{cut}} = 186 \pm 14$ keV, consistent with yet more precise than the measurement from paper I) is consistent with that obtained by Molina et al. (2009), as discussed in § 4.2. It is also at the median point of the high-energy power-law cutoffs that have been measured in Seyfert AGN thus far with *NuSTAR*. Others include Ark 120 (≥ 190 keV, Matt et al. 2014), SWIFT J2127.4+5654 (108^{+11}_{-10} keV, Marinucci et al. 2014) and Mrk 335 (≥ 153 keV, Parker et al., submitted).

Owing to the high quality and broadband energy coverage of our data, we were able to reach beyond the phenomenological power-law representation of the continuum and consider more physical models, following our work with the *NuSTAR* data alone in paper I. Models 2-3 provide roughly equivalent statistical fits to the data, incorporating a **compTT** model that parametrizes the temperature, optical depth and geometry of the electron plasma, as well as an **xillver** model that assumes a neutral slab of material inclined at 60° to our line of sight and leaves the reflected flux from the disk and its iron abundance as free parameters. We also added in two Gaussian components to represent (1) a blend of the resonance, intercombination and forbidden O VII emission lines, and (2) a contribution from a broad Fe $K\alpha$ line from the inner disk.

The goodness-of-fit is largely insensitive to the coronal geometry assumed, though the temperatures derived from the spherical and slab geometries are inconsistent at the $> 2\sigma$ level ($kT = 50^{+6}_{-3}$ keV and $kT = 61 \pm 1$ keV, respectively). The two models also produce different values for the optical depth of the corona: $\tau = 2.34^{+0.16}_{-0.21}$ and $\tau = 0.68 \pm 0.02$, respectively. These values differ by $> 4\sigma$ (see Fig. 12) even after the factor-of-two geometrical difference in calculating the optical depth is accounted for (see paper I), indicating that a physical change in the properties of the plasma is necessary when applying a different geometry in order to achieve a good fit. This was not the case when Models 2-3 were fit to the *NuSTAR* data alone in paper I. Unfortunately, the lack of both short timescale variability and significant relativistic, inner disk reflection in IC 4329A during our observing campaign prevents us from determining the distance of the corona from the accretion disk, and from being able to constrain how centrally concentrated the coronal emission is.

Though the spherical model returns a slightly better statistical fit, we conclude that the slab model is more physically believable due to the tighter match it provides between

coronal temperature and power-law cutoff energy (assuming $E_{\text{cut}} \sim 2 - 3kT$; in this case, $3kT = 183 \pm 3 \text{ keV}$, which is much closer than Model 2 to being compatible with the measured power-law cutoff value in Model 1). We also note that the temperature and optical depth of the plasma are much more tightly constrained in the slab geometry. Due to an inherent modeling degeneracy between the optical depth and temperature of the electron plasma in each geometry, however, there is a small, linearly correlated range of values for these parameters which demonstrate approximately equal statistical fit quality, as can be seen in Figs. 8a and 9a. It is thus not surprising that, as the temperature increases in the slab vs. sphere case, the optical depth decreases to compensate and produce an equivalent goodness-of-fit. Nonetheless, both parameters are constrained with the best precision and accuracy ever achieved.

We also note that both sets of values for the coronal temperature and optical depth measured with the combined, simultaneous *Suzaku* and *NuSTAR* datasets deviate significantly from those obtained when fitting the *NuSTAR* data alone in Models 2-3 of paper I (Figs. 8a, 9a and 12). In particular, the slab geometry in paper I returned $kT_e = 37_{-6}^{+7} \text{ keV}$ and $\tau = 1.25_{-0.10}^{+0.20}$, which is inconsistent with the results for this geometry using the combined dataset at a $> 3\sigma$ level. We attribute this difference to the larger spectral energy coverage of the combined dataset, which, as noted previously, allows us to definitively disentangle the signatures of the continuum, reflection and absorption in ways that *NuSTAR* alone cannot, since its effective area only extends down to 3 keV and its spectral resolution in the Fe K band is three times worse than that of *Suzaku* (450 eV vs. 150 eV). The amount of reflection in the system and the curvature induced by the high-energy cutoff of the continuum are particularly degenerate at energies $> 10 \text{ keV}$, but having the high-S/N, high spectral resolution *Suzaku* data in the Fe K band, especially, allows us to break this degeneracy and to independently constrain kT_e and K_{refl} (see Figs. 8b and 9b). Taking these factors into account, we consider the values for the coronal temperature and optical depth measured in this work to be the definitive physical properties of the corona in IC 4329A. Their deviation from those determined through the analysis of only $> 3 \text{ keV}$ data at lower spectral resolution underscore the importance of obtaining high-S/N data across a broad X-ray bandpass in order to draw conclusions about the corona from Comptonization models.

As more constraints on coronal parameters are measured from a sample of AGN, it will be interesting to compare the coronal properties (e.g., Γ , kT , τ) with the those of the black hole and inner accretion flow (e.g., M_{BH} , a , \dot{m}). It has long been thought that more actively accreting black holes cool their coronae more efficiently (Skipper, Mc Hardy, & Maccarone 2013 and references therein), but a sample of AGN with sensitive, broad-band X-ray spectra, as presented here for IC 4329A, would help to test this conjecture.

5.3. The Fe K Region

The addition of the *Suzaku* data enables us to perform a detailed analysis of the Fe K region in IC 4329A, while the *NuSTAR* data provide an important check on the physical consistency of our models by simultaneously showing us the Compton reflection continuum > 10 keV. The majority of the reflection component originates in material at large distances from the black hole (e.g., the putative torus), and is well fit by a static, neutral **xillver** component. Though there is evidence for a broad Fe K α line or a Compton shoulder due to the residuals remaining after a narrow Fe K α line is included, the broad line explanation is more likely since the reflection models we employ already incorporate a Compton shoulder component. That said, the Compton shoulder explanation cannot be conclusively ruled out with these data.

Assuming that the residuals do correspond to a broad iron line component, modeling this emission feature with a relativistic line profile (e.g., **diskline**, **laor** or **relline**) yields no improvement in the fit and the model parameters cannot be constrained. We have successfully modeled this residual emission with a Gaussian line at $E \sim 6.4$ keV, and can place a limit on its strength relative to the continuum of $EW = 24 - 42$ eV (Model 1). Only $\sim 1\%$ of the reflected emission arises from the broadened Fe K α feature. While obviously present and originating from well within the broad emission line region ($v_{\text{FWHM}} \sim 36,000 \text{ km s}^{-1}$), this feature likely represents only a weak broad line from the inner disk. Indeed, the reflection fraction constrained via the **pexrav** model in §4.1 is also low by comparison with other bright, nearby Seyfert 1 AGN (Walton et al. 2013). Such a finding is in keeping with the theoretical work of Ballantyne (2010), however, who suggested that the majority of Seyferts may have broad Fe K α lines with $EW \leq 100$ eV. Our inability to constrain any of the parameters when a relativistic disk line model is applied renders it useless in constraining the spin of the black hole, however. Similarly, attempting to fit this feature with a relativistic smearing kernel convolved with an ionized disk reflection spectrum also results in no statistical improvement in fit and no parameter constraints. The feature is not apparent in the high-low flux difference spectrum of the AGN, meaning that it is not significantly variable over the course of the observations. Even if it does arise from inner disk reflection this is not surprising, given the lack of short timescale variability of the continuum.

A broad Fe K line has been reported in every observation taken of IC 4329A with an X-ray observatory capable of spectrally resolving it (Piro et al. 1990; Madejski et al. 1995; Cappi et al. 1996; Perola et al. 1999; Done et al. 2000; Gondoin et al. 2001; McKernan & Yaqoob 2004; Steenbrugge et al. 2005; Markowitz et al. 2006; Dadina 2007; Molina et al. 2009, 2013). Such a line was also noted in the *XMM-Newton* analysis of the source by de La Calle Pérez et al. (2010), suggesting that this line, though difficult to characterize

definitively, is a persistent feature of the spectrum over years-long timescales. Provided that sufficient photon counts have been obtained in the observation (i.e., $\geq 200,000$ from $2 - 10$ keV), broad Fe K lines are detected in $\geq 40\%$ of all AGN (Guainazzi, Bianchi, & Dovčiak 2006; Nandra et al. 2007; de La Calle Pérez et al. 2010). Further, some actively accreting AGN have had broad Fe K emission lines reported in previous epochs but not currently (e.g., NGC 5548, Brenneman et al. 2012). Taking these points into consideration, it is perhaps not surprising to find that IC 4329A does not exhibit strong relativistic reflection signatures during our observation. Indeed, marginal detections of broad Fe K emission lines such as that found here may be the norm rather than the exception among even actively accreting AGN (Ballantyne 2010). Within this framework, it is intriguing to note that the source is accreting at $L_{\text{bol}}/L_{\text{Edd}} \sim 0.46$ for a black hole with an estimated mass of $M_{\text{BH}} = 1.20 \times 10^8 M_{\odot}$ (de La Calle Pérez et al. 2010). Given that the Keplerian velocity of the broadened Fe K α feature places its origin at $r \sim 70 r_{\text{g}}$ from the black hole, this suggests that the optically thick disk may not extend down to the ISCO. The disk may be truncated within this radius, or perhaps it is too highly ionized to significantly contribute to the reflection spectrum. Indeed, highly ionized disks are expected in relatively high accretion rate sources (Ballantyne, McDuffie, & Rusin 2011) such as IC 4329A. The power-law photon index of the source is also considerably harder ($\Gamma \sim 1.73$) than is typical for an actively accreting source with an inner disk extending down to its ISCO, and marks a departure of $> 6\sigma$ from the AGN relation measured by Brightman et al. (2013). According to these authors, for an Eddington ratio of $L_{\text{bol}}/L_{\text{Edd}} = 0.46$, one should measure $\Gamma = 2.16 \pm 0.07$, in contrast to the $\Gamma = 1.73 \pm 0.01$ measured here for IC 4329A (however, the intrinsic scatter in this relation must be considered, as must the uncertainty in measuring the Eddington ratio in a given source).

The relative weakness of the reflection features compared to similar AGN coupled with the hard power-law index of the source, particularly, lends credence to the hypothesis put forward in paper I: that we are witnessing an outflowing corona with $v_{\text{out}} \sim 0.2c$, following the work of Beloborodov (1999) and Malzac, Beloborodov, & Poutanen (2001). Although an ionized inner disk would certainly inhibit strong reflection features from this region, as per Ballantyne (2010), it is worth noting that the outflowing corona scenario would suppress them as well: if the main locus of coronal emission is situated at a height of $\geq 50 r_{\text{g}}$ then we become insensitive to reflection from the disk within $50 r_{\text{g}}$. Also, if the corona is relativistically outflowing then aberration decreases the illumination of the inner disk, again making us less sensitive to any reflection from this region. Under any of the above conditions we would not expect to be able to constrain the spin of the black hole in IC 4329A. A deep multi-wavelength campaign involving UV spectra, particularly, in addition to the outstanding data now available in X-rays with *NuSTAR* and *Suzaku*, *XMM-Newton* or *Chandra* would

be necessary in order to properly evaluate the characteristics and structure of the inner accretion disk, and to place our results on the energetics of the system in their proper context.

This work was supported under NASA Contract No. NNG08FD60C, and made use of data from the *NuSTAR* mission, a project led by the California Institute of Technology, managed by the Jet Propulsion Laboratory, and funded by the National Aeronautics and Space Administration. We thank the *NuSTAR* Operations, Software and Calibration teams for support with the execution and analysis of these observations. This research has made use of the *NuSTAR* Data Analysis Software (NuSTARDAS) jointly developed by the ASI Science Data Center (ASDC, Italy) and the California Institute of Technology (USA). LB thanks Koji Mukai and the *Suzaku* GOF at NASA/GSFC for all their assistance in obtaining and analyzing that data, and also gratefully acknowledges funding from NASA grant NNX13AE90G. G. Matt and AM acknowledge financial support from Italian Space Agency under contract ASI/INAF I/037/12/0 - 011/13.

REFERENCES

- Antonucci, R. 1993, ARA&A, 31, 473
- Arnaud, K. A. 1996, in Astronomical Society of the Pacific Conference Series, Vol. 101, Astronomical Data Analysis Software and Systems V, ed. G. H. Jacoby & J. Barnes, 17
- Ballantyne, D. R. 2010, ApJ, 708, L1
- Ballantyne, D. R., McDuffie, J. R., & Rusin, J. S. 2011, ApJ, 734, 112
- Beckmann, V., Gehrels, N., Shrader, C. R., & Soldi, S. 2006, ApJ, 638, 642
- Beloborodov, A. M. 1999, ApJ, 510, L123
- Boldt, E. 1987, Phys. Rep., 146, 215
- Brenneman, L. 2013, Measuring the Angular Momentum of Supermassive Black Holes (Springer)
- Brenneman, L. W., Elvis, M., Krongold, Y., Liu, Y., & Mathur, S. 2012, ApJ, 744, 13

- Brenneman, L. W., Madejski, G., Fuerst, F., Matt, G., Elvis, M., Harrison, F. A., Ballantyne, D. R., Boggs, S. E., et al. 2014, *ApJ*, 781, 83
- Brightman, M., Silverman, J. D., Mainieri, V., Ueda, Y., Schramm, M., Matsuoka, K., Nagao, T., Steinhardt, C., et al. 2013, *MNRAS*, 433, 2485
- Cappi, M., Mihara, T., Matsuoka, M., Hayashida, K., Weaver, K. A., & Otani, C. 1996, *ApJ*, 458, 149
- Dadina, M. 2007, *A&A*, 461, 1209
- Dauser, T., Wilms, J., Reynolds, C. S., & Brenneman, L. W. 2010, *MNRAS*, 409, 1534
- de La Calle Pérez, I., Longinotti, A. L., Guainazzi, M., Bianchi, S., Dovčiak, M., Cappi, M., Matt, G., Miniutti, G., et al. 2010, *A&A*, 524, A50
- Done, C., Madejski, G. M., & Życki, P. T. 2000, *ApJ*, 536, 213
- Edelson, R., Turner, T. J., Pounds, K., Vaughan, S., Markowitz, A., Marshall, H., Dobbie, P., & Warwick, R. 2002, *ApJ*, 568, 610
- García, J., Dauser, T., Lohfink, A., Kallman, T. R., Steiner, J. F., McClintock, J. E., Brenneman, L., Wilms, J., et al. 2014, *ApJ*, 782, 76
- Gondoin, P., Barr, P., Lumb, D., Oosterbroek, T., Orr, A., & Parmar, A. N. 2001, *A&A*, 378, 806
- Guainazzi, M., Bianchi, S., & Dovčiak, M. 2006, *Astronomische Nachrichten*, 327, 1032
- Harrison, F. A., Craig, W. W., Christensen, F. E., Hailey, C. J., Zhang, W. W., Boggs, S. E., Stern, D., Cook, W. R., et al. 2013, *ApJ*, 770, 103
- Kalberla, P. M. W., Burton, W. B., Hartmann, D., Arnal, E. M., Bajaja, E., Morras, R., & Pöppel, W. G. L. 2005, *A&A*, 440, 775
- Kallman, T. & Bautista, M. 2001, *ApJS*, 133, 221
- Kashyap, V. & Drake, J. J. 1998, *ApJ*, 503, 450
- Longair, M. S. 2011, *High Energy Astrophysics*, Cambridge University Press
- Lubiński, P., Zdziarski, A. A., Walter, R., Paltani, S., Beckmann, V., Soldi, S., Ferrigno, C., & Courvoisier, T. J.-L. 2010, *MNRAS*, 408, 1851
- Madejski, G., Done, C., & Życki, P. 2001, *Advances in Space Research*, 28, 369

- Madejski, G. M., Zdziarski, A. A., Turner, T. J., Done, C., Mushotzky, R. F., Hartman, R. C., Gehrels, N., Connors, A., et al. 1995, *ApJ*, 438, 672
- Magdziarz, P. & Zdziarski, A. A. 1995, *MNRAS*, 273, 837
- Malzac, J., Beloborodov, A. M., & Poutanen, J. 2001, *MNRAS*, 326, 417
- Marinucci, A., Matt, G., Kara, E., Miniutti, G., Elvis, M., Arevalo, P., Ballantyne, D. R., Balokovic, M., et al. 2014, *ArXiv e-prints*
- Marinucci, A., Risaliti, G., Wang, J., Nardini, E., Elvis, M., Fabbiano, G., Bianchi, S., & Matt, G. 2012, *MNRAS*, 423, L6
- Markowitz, A. 2009, *ApJ*, 698, 1740
- Markowitz, A. & Edelson, R. 2004, *ApJ*, 617, 939
- Markowitz, A., Reeves, J. N., & Braitto, V. 2006, *ApJ*, 646, 783
- Matt, G., Marinucci, A., Guainazzi, M., Brenneman, L. W., Elvis, M., Lohfink, A., Arevalo, P., Boggs, S. E., et al. 2014, *MNRAS*, 439, 3016
- McKernan, B. & Yaqoob, T. 2004, *ApJ*, 608, 157
- Miyazawa, T., Haba, Y., & Kunieda, H. 2009, *PASJ*, 61, 1331
- Molina, M., Bassani, L., Malizia, A., Stephen, J. B., Bird, A. J., Bazzano, A., & Ubertini, P. 2013, *MNRAS*, 433, 1687
- Molina, M., Bassani, L., Malizia, A., Stephen, J. B., Bird, A. J., Dean, A. J., Panessa, F., de Rosa, A., et al. 2009, *MNRAS*, 399, 1293
- Nandra, K., O’Neill, P. M., George, I. M., & Reeves, J. N. 2007, *MNRAS*, 382, 194
- Niedźwiecki, A. & Miyakawa, T. 2010, *A&A*, 509, A22
- Perola, G. C., Matt, G., Cappi, M., Dal Fiume, D., Fiore, F., Guainazzi, M., Mineo, T., Molendi, S., et al. 1999, *A&A*, 351, 937
- Perola, G. C., Matt, G., Cappi, M., Fiore, F., Guainazzi, M., Maraschi, L., Petrucci, P. O., & Piro, L. 2002, *A&A*, 389, 802
- Piro, L., Yamauchi, M., & Matsuoka, M. 1990, *ApJ*, 360, L35
- Reynolds, C. S. 2013, *Space Sci. Rev.*

- Risaliti, G., Harrison, F. A., Madsen, K. K., Walton, D. J., Boggs, S. E., Christensen, F. E., Craig, W. W., Grefenstette, B. W., et al. 2013, *Nature*, 494, 449
- Shu, X. W., Yaqoob, T., & Wang, J. X. 2010, *ApJS*, 187, 581
- Skipper, C. J., McHardy, I. M., & Maccarone, T. J. 2013, *MNRAS*, 434, 574
- Sobolewska, M. A. & Papadakis, I. E. 2009, *MNRAS*, 399, 1597
- Soldi, S., Beckmann, V., Baumgartner, W. H., Ponti, G., Shrader, C. R., Lubiński, P., Krimm, H. A., Mattana, F., et al. 2014, *A&A*, 563, A57
- Steenbrugge, K. C., Kaastra, J. S., Sako, M., Branduardi-Raymont, G., Behar, E., Paerels, F. B. S., Blustin, A. J., & Kahn, S. M. 2005, *A&A*, 432, 453
- Tanaka, Y., Nandra, K., Fabian, A. C., Inoue, H., Otani, C., Dotani, T., Hayashida, K., Iwasawa, K., et al. 1995, *Nature*, 375, 659
- Titarchuk, L. 1994, *ApJ*, 434, 570
- Urry, C. M. & Padovani, P. 1995, *PASP*, 107, 803
- Vaughan, S., Edelson, R., Warwick, R. S., & Uttley, P. 2003, *MNRAS*, 345, 1271
- Verner, D. A., Ferland, G. J., Korista, K. T., & Yakovlev, D. G. 1996, *ApJ*, 465, 487
- Verrecchia, F., in’t Zand, J. J. M., Giommi, P., Santolamazza, P., Granata, S., Schuurmans, J. J., & Antonelli, L. A. 2007, *A&A*, 472, 705
- Walton, D. J., Nardini, E., Fabian, A. C., Gallo, L. C., & Reis, R. C. 2013, *MNRAS*, 428, 2901
- Willmer, C. N. A., Focardi, P., Chan, R., Pellegrini, P. S., & da Costa, N. L. 1991, *AJ*, 101, 57
- Wilms, J., Allen, A., & McCray, R. 2000, *ApJ*, 542, 914
- Wilson, A. S. & Penston, M. V. 1979, *ApJ*, 232, 389
- Yaqoob, T. & Padmanabhan, U. 2004, *ApJ*, 604, 63
- Zdziarski, A. A., Gierlinski, M., Gondek, D., & Magdziarz, P. 1996, *A&AS*, 120, C553
- Zdziarski, A. A. *et al.* 1994, *MNRAS*, 269, L55

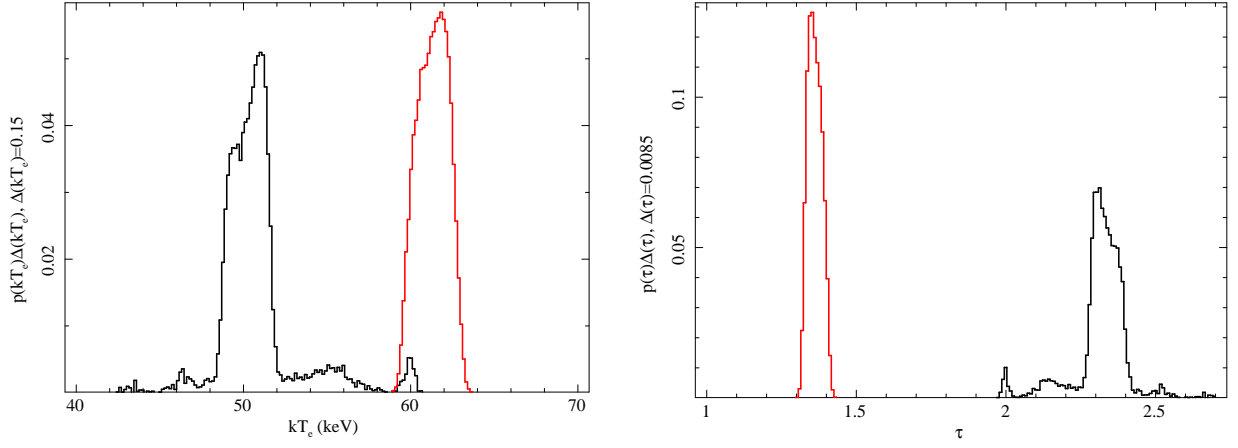


Fig. 12.— *Left:* Probability density for the `compTT` electron temperature (kT_e) in the spherical (black) and slab (red) geometries, as determined from our MCMC analysis. *Right:* The same plot, this time for the optical depth (τ) of the electrons. The optical depths for the slab geometry have been multiplied by a factor of two (see paper I) to make them more directly comparable to the optical depths measured in the spherical geometry.